End-to-end distance probability distributions of dilute polyethylene oxide in aqueous solution

Nicholas Sherck[1], Thomas Webber[1], Dennis Robinson Brown[1], Timothy Keller[2], Mikayla Barry[3], Audra DeStefano[1], Sally Jiao[1], Rachel A. Segalman[1,3], Glenn H. Fredrickson[1,3,4], M. Scott Shell[1*], Songi Han[1,2,*]

[1]Department of Chemical Engineering, University of California, Santa Barbara, California 93106 U.S.A.
[2]Department of Chemistry and Biochemistry, University of California, Santa Barbara, California, 93106 U.S.A.
[3]Department of Materials, University of California, Santa Barbara, California, 93106 U.S.A.
[4]Materials Research Laboratory, University of California, Santa Barbara, California 93106 USA

*Corresponding authors. Email: shell@ucsb.edu; songi@chem.ucsb.edu.

Contents

Section 1: Experimental PEO details....3

Section 1a: Polydispersity of the PEO samples....3

Section 1b: MALDI characterization of PEO samples 4

Section 1c: Spin-labeling reaction 6

Section 1d: PEO NMR Spectroscopic Data....7

Section 2: DEER experimental limitations and analysis....12

Section 2a: DEER limitations at short distances 12

Section 2b: DEER data analysis....14

Section 3: The GaFF2 force-field and 4-site OPC water model....15

Section 3a: Charging the unlabeled PEO polymer....15

Section 3b: Charging the spin probe labeled PEO 18

Section 3c: PEO solution densities 21

Section 4: Molecular dynamics simulation protocol 22

Section 5: Convergence of labeled to unlabeled PEO $\underline{Ree}$ values....24

Section 6: Spin-probe Aggregation....25

Section 7:....27

Section 7a: $\underline{Ree}$ average values compared to other literature models....27

Section 7b: $\underline{Ree}$ and $\underline{Rg}$ data from scattering experiments 28

Section 7c: $\underline{Ree}$ Correlation Times 29

Section 8: $\underline{Rg}$ values....30

Section 8a: $\underline{Rg}$ values compared to light scattering data 30

Section 8b: $\underline{Rg}$ values compared to other PEO literature models 31

Section 9: $\underline{Ree}$ vs. molecular weight fits 32

Section 10: PEO persistence length and characteristic ratio from simulation 33

Section 11: Radial distribution functions and water hydration....34

Section 12: 1,2-dimethoxyethane dihedral populations and helicity....36

Section 13: $\underline{\alpha}$ 37

Section 14: Scaled distribution moments....38

Section 15: References....39

Section 1: Experimental PEO details

Section 1a: Polydispersity of the PEO samples

Gel permeation chromatography (GPC) traces for PEO 36-mer and 59-mer were measured before they were spin-labeled. Both show narrow dispersity (Đ) indicating variations in end-to-end distances are likely not due to variations in molecular weight. The three smallest PEO samples (5-mer, 13-mer, and 25-mer) were purchased with known monomer counts and were small enough to not necessitate GPC analysis.

PEO Sample	M_w (g/mol)	M_n (g/mol)	Đ
36-mer	2850 ± 17.8%	2800 ± 17.9%	1.017
59-mer	4010 ± 18.1%	3950 ± 18.4%	1.015

Table S01. GPC-derived molecular weights for PEO 36-mer and 59-mer.

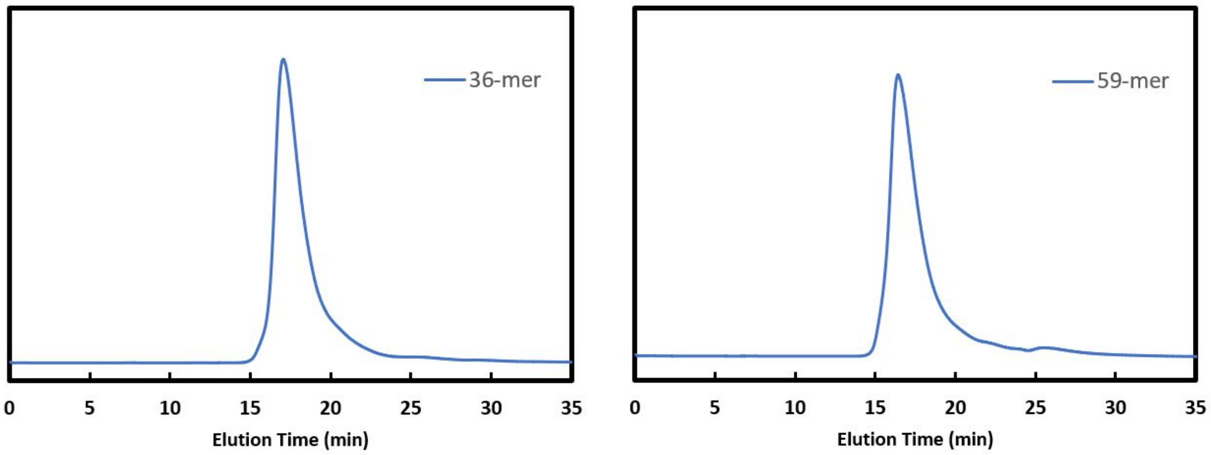

Figure S01. GPC traces for PEO 36-mer and 59-mer.

Section 1b: MALDI characterization of PEO samples

Matrix-assisted laser desorption ionization mass spectrometry (MALDI-MS) was performed for PEO 36-mer and 59-mer after they were spin-labeled. This was done on a Bruker Microflex LRF MALDI TOF mass spectrometer. Alpha-cyano matrix was prepared in 1:1 vol/vol HPLC-quality water and acetonitrile. Matrix-sample mixtures were spotted onto a polished steel MALDI target plate. Mass spectra are the average of at least 500 points collected in positive reflectron mode. The peak molecular weight for PEO 36-mer is 2572 g/mol and for PEO 59-mer is 3660 g/mol. The other fractions of polymer mass show a relatively narrow dispersity, in agreement with the GPC.

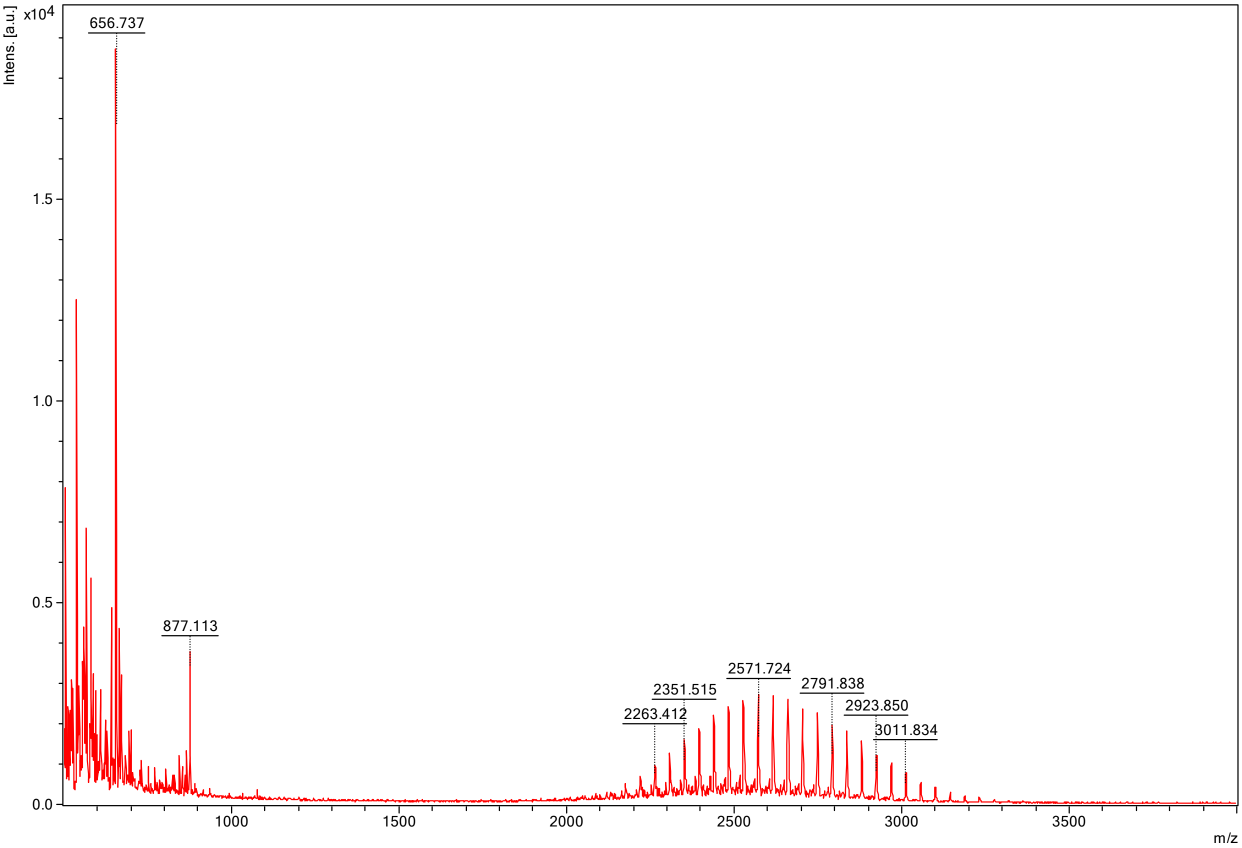

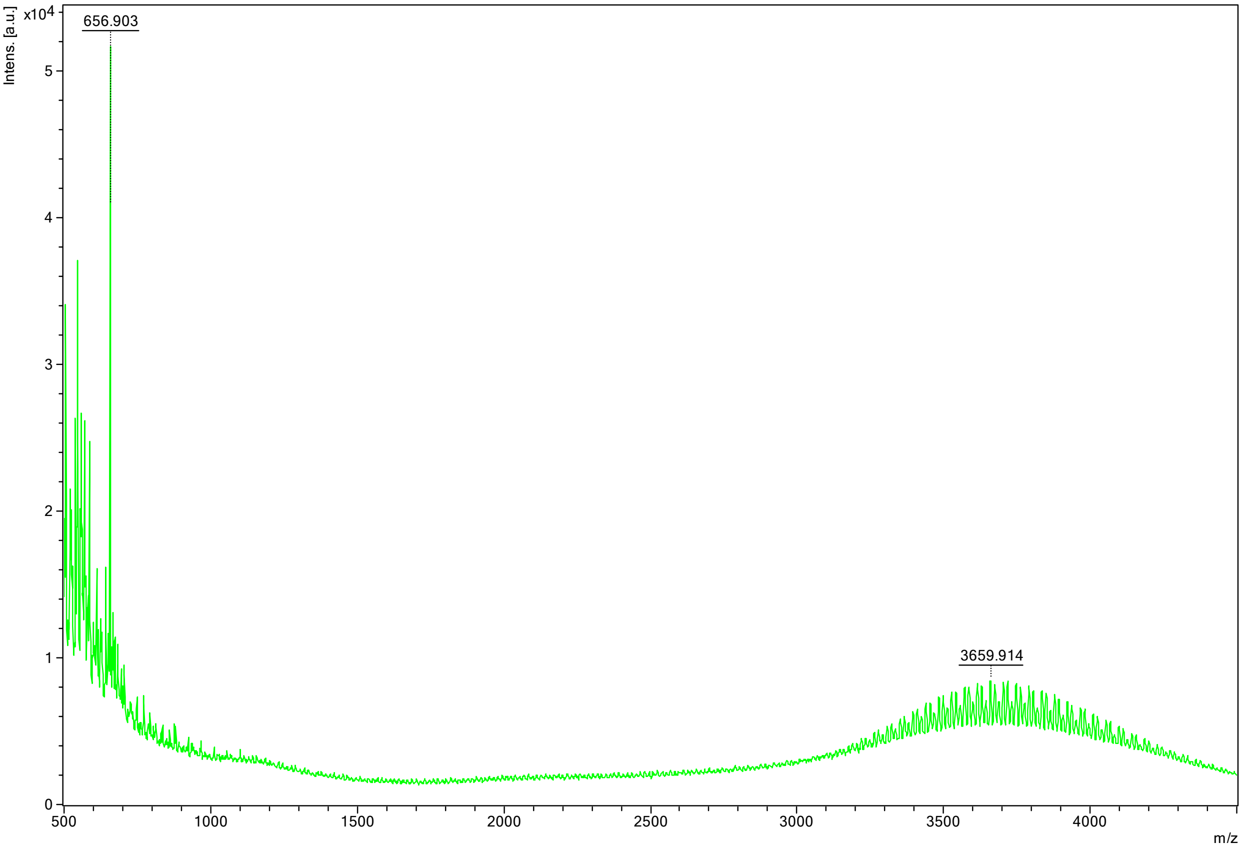

Figure S02. MALDI traces for spin-labeled PEO 36-mer (upper in red) and 59-mer (lower in green). The x-axis is mass/charge (m/z) and values can be interpreted as molecular weight (g/mol).

Section 1c: Spin-labeling reaction

The reaction scheme described in the Methods section is displayed in Figure S02. The NHS esters on each end of the PEO reacted with the primary amine on 4-amino-TEMPO, yielding a stable amide bond between PEO and TEMPO. The reaction was performed in tetrahydrofuran (THF) and catalyzed with triethylamine (TEA) and stirred at room temperature overnight.

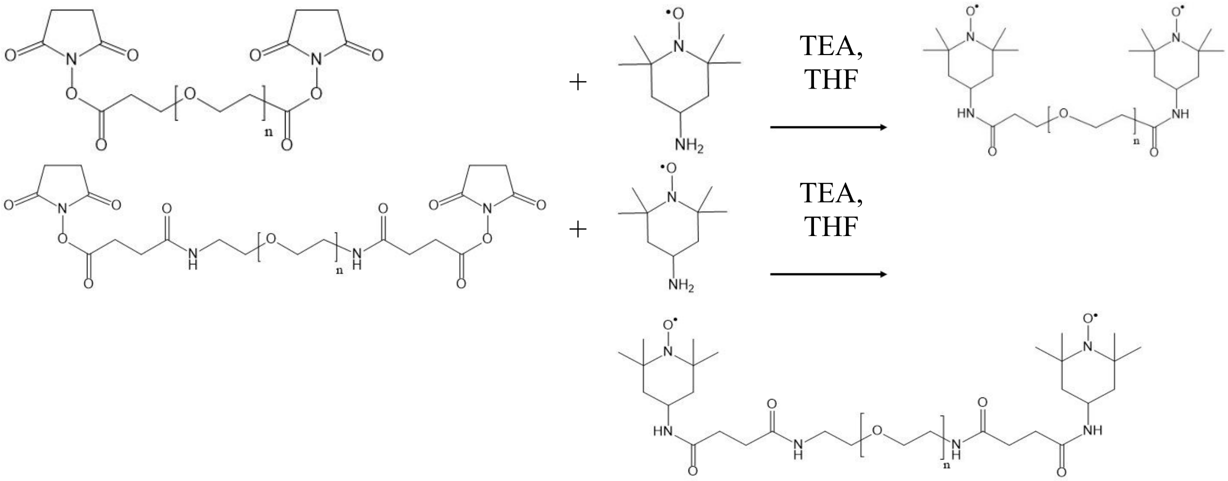

Figure S03: Spin-labeling reaction for PEO lengths is n= 5, 13, and 25 for the upper reaction, and n=36 and 59 for the lower reaction.

Section 1d: PEO NMR Spectroscopic Data

NMR spectroscopic data was obtained for all five unlabeled PEO samples used in this study.

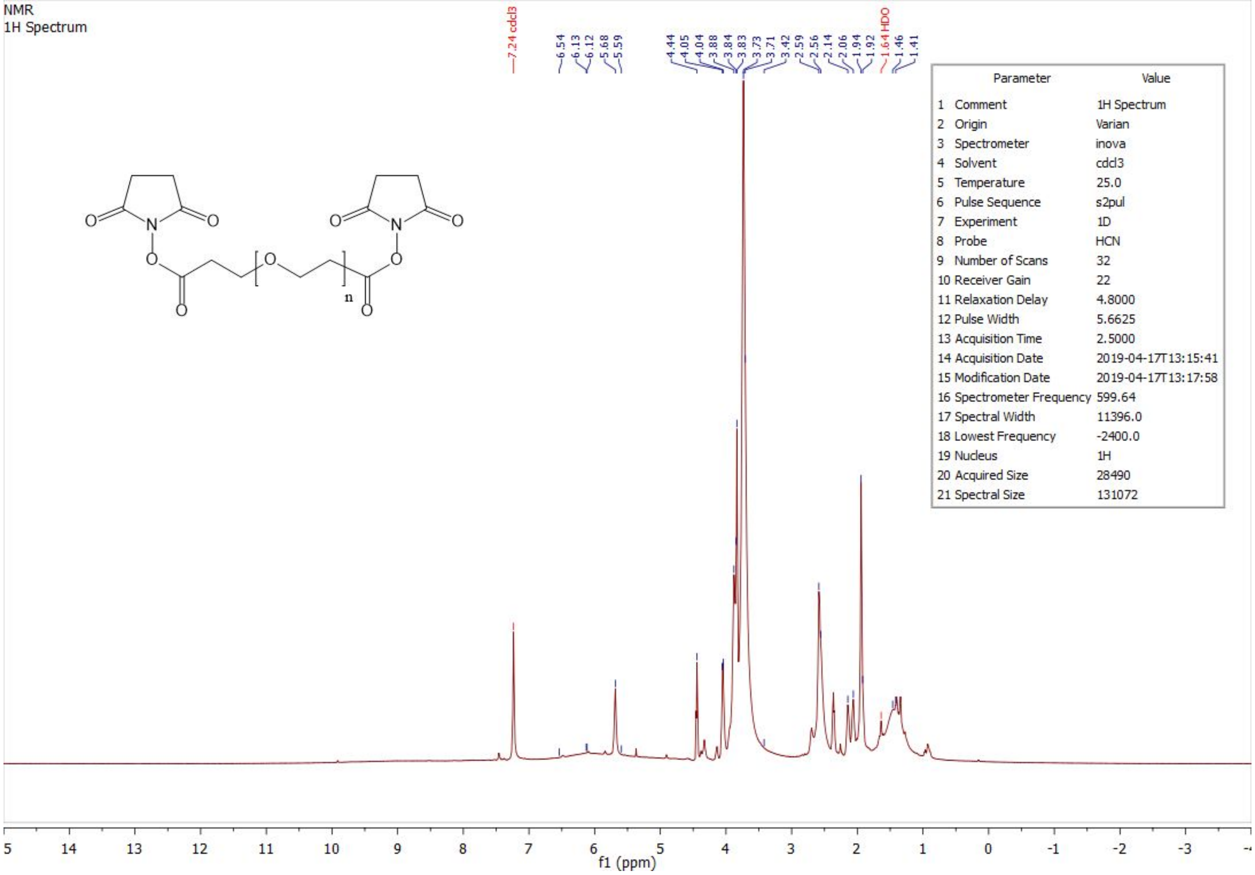

	Parameter	Value
1	Comment	1H Spectrum
2	Origin	Varian
3	Spectrometer	inova
4	Solvent	cdcl3
5	Temperature	25.0
6	Pulse Sequence	s2pul
7	Experiment	1D
8	Probe	HCN
9	Number of Scans	32
10	Receiver Gain	22
11	Relaxation Delay	4.8000
12	Pulse Width	5.6625
13	Acquisition Time	2.5000
14	Acquisition Date	2019-04-17T13:15:41
15	Modification Date	2019-04-17T13:17:58
16	Spectrometer Frequency	599.64
17	Spectral Width	11396.0
18	Lowest Frequency	-2400.0
19	Nucleus	1H
20	Acquired Size	28490
21	Spectral Size	131072

Figure S04: ^{1}H NMR spectrum obtained for PEO 5-mer

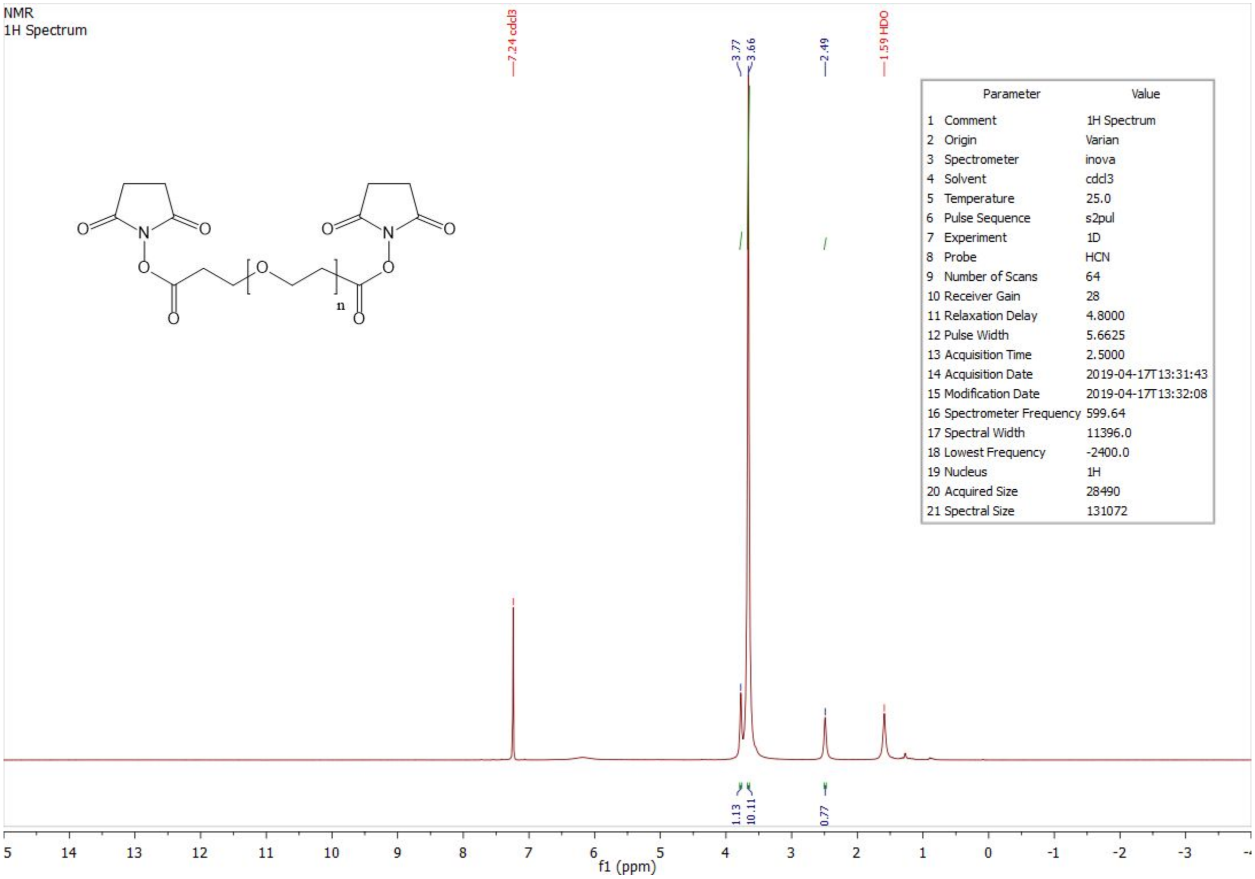

	Parameter	Value
1	Comment	1H Spectrum
2	Origin	Varian
3	Spectrometer	inova
4	Solvent	cdcl3
5	Temperature	25.0
6	Pulse Sequence	s2pul
7	Experiment	1D
8	Probe	HCN
9	Number of Scans	64
10	Receiver Gain	28
11	Relaxation Delay	4.8000
12	Pulse Width	5.6625
13	Acquisition Time	2.5000
14	Acquisition Date	2019-04-17T13:31:43
15	Modification Date	2019-04-17T13:32:08
16	Spectrometer Frequency	599.64
17	Spectral Width	11396.0
18	Lowest Frequency	-2400.0
19	Nucleus	1H
20	Acquired Size	28490
21	Spectral Size	131072

Figure S05: ^{1}H NMR spectrum obtained for PEO 13-mer

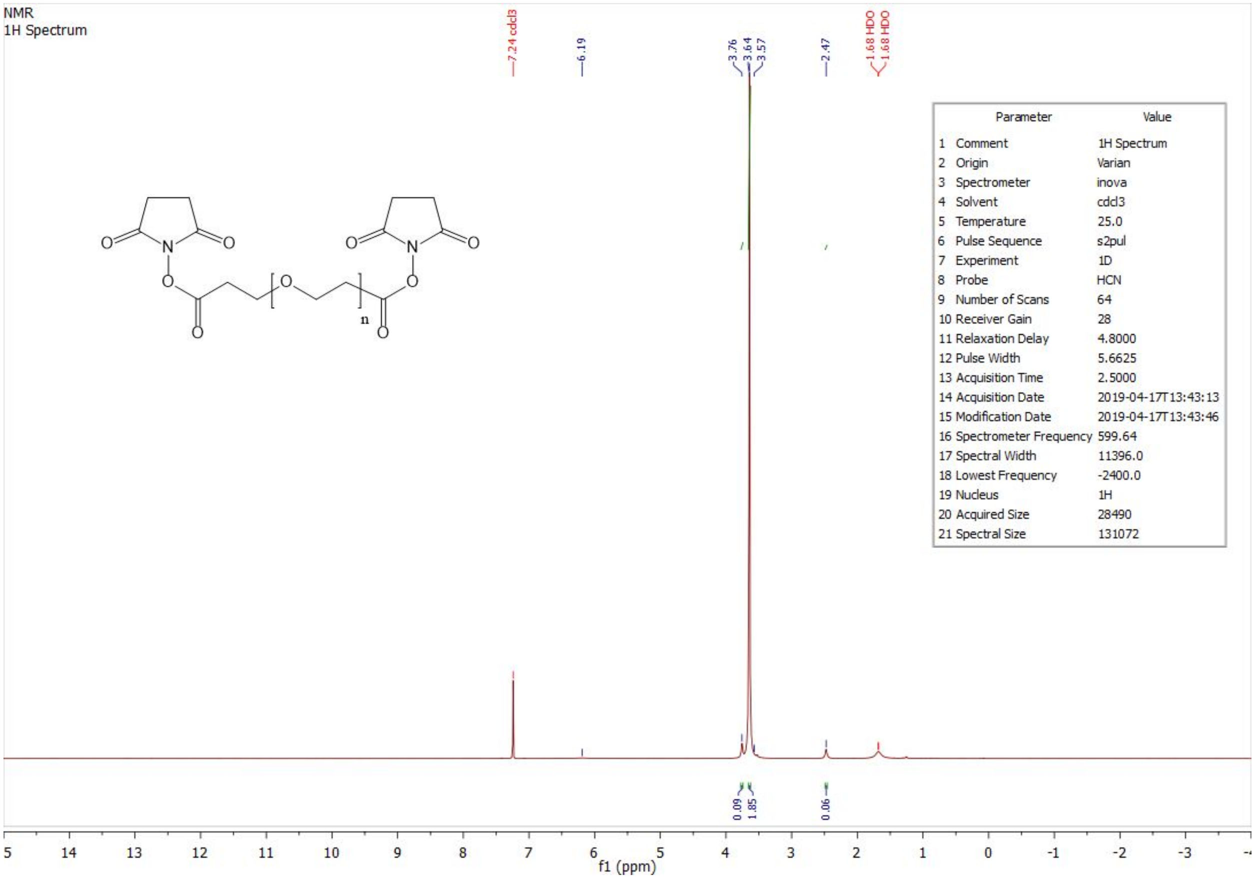

Parameter	Value
1 Comment	1H Spectrum
2 Origin	Varian
3 Spectrometer	inova
4 Solvent	cdcl3
5 Temperature	25.0
6 Pulse Sequence	s2pul
7 Experiment	1D
8 Probe	HCN
9 Number of Scans	64
10 Receiver Gain	28
11 Relaxation Delay	4.8000
12 Pulse Width	5.6625
13 Acquisition Time	2.5000
14 Acquisition Date	2019-04-17T13:43:13
15 Modification Date	2019-04-17T13:43:46
16 Spectrometer Frequency	599.64
17 Spectral Width	11396.0
18 Lowest Frequency	-2400.0
19 Nucleus	1H
20 Acquired Size	28490
21 Spectral Size	131072

Figure S06: ^{1}H NMR spectrum obtained for PEO 25-mer

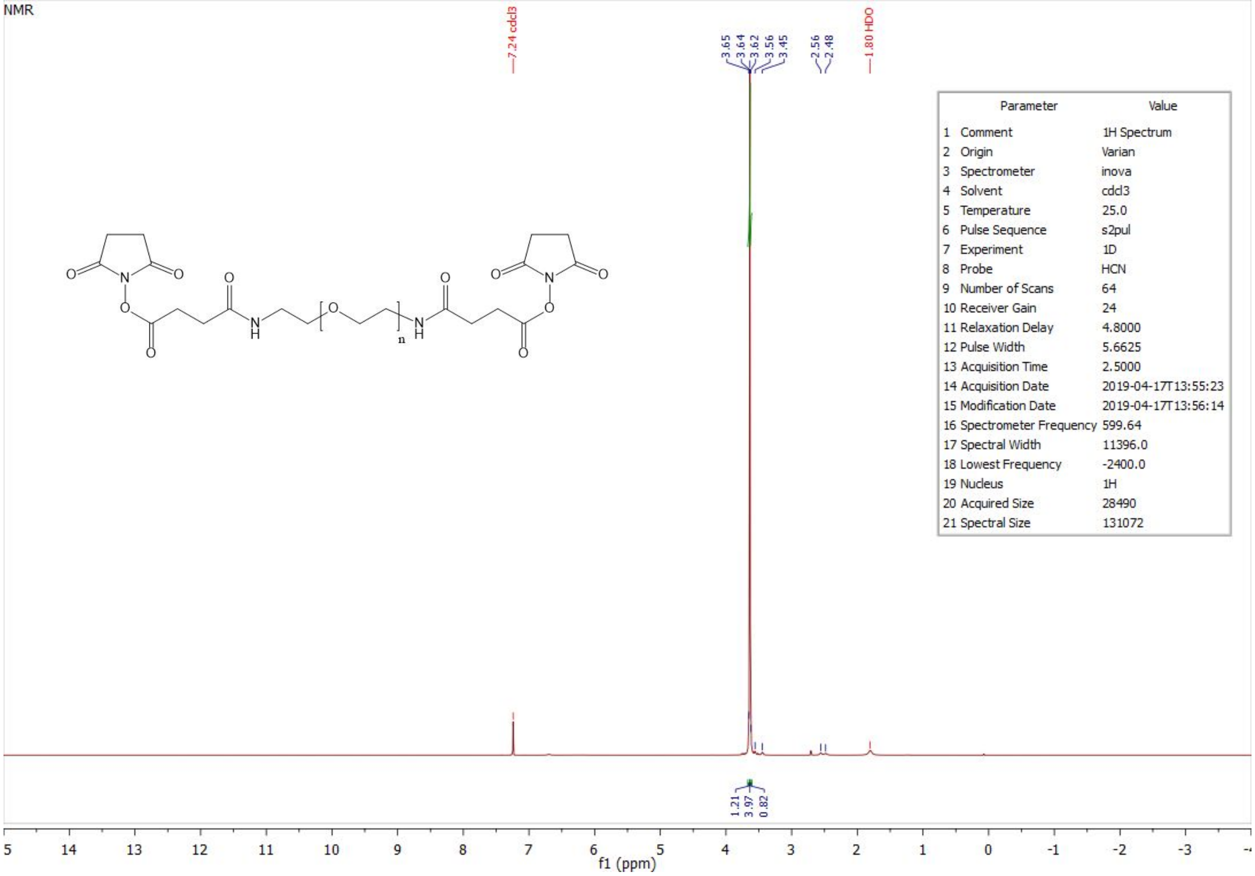

	Parameter	Value
1	Comment	1H Spectrum
2	Origin	Varian
3	Spectrometer	inova
4	Solvent	cdcl3
5	Temperature	25.0
6	Pulse Sequence	s2pul
7	Experiment	1D
8	Probe	HCN
9	Number of Scans	64
10	Receiver Gain	24
11	Relaxation Delay	4.8000
12	Pulse Width	5.6625
13	Acquisition Time	2.5000
14	Acquisition Date	2019-04-17T13:55:23
15	Modification Date	2019-04-17T13:56:14
16	Spectrometer Frequency	599.64
17	Spectral Width	11396.0
18	Lowest Frequency	-2400.0
19	Nucleus	1H
20	Acquired Size	28490
21	Spectral Size	131072

Figure S07: ^{1}H NMR spectrum obtained for PEO 36-mer

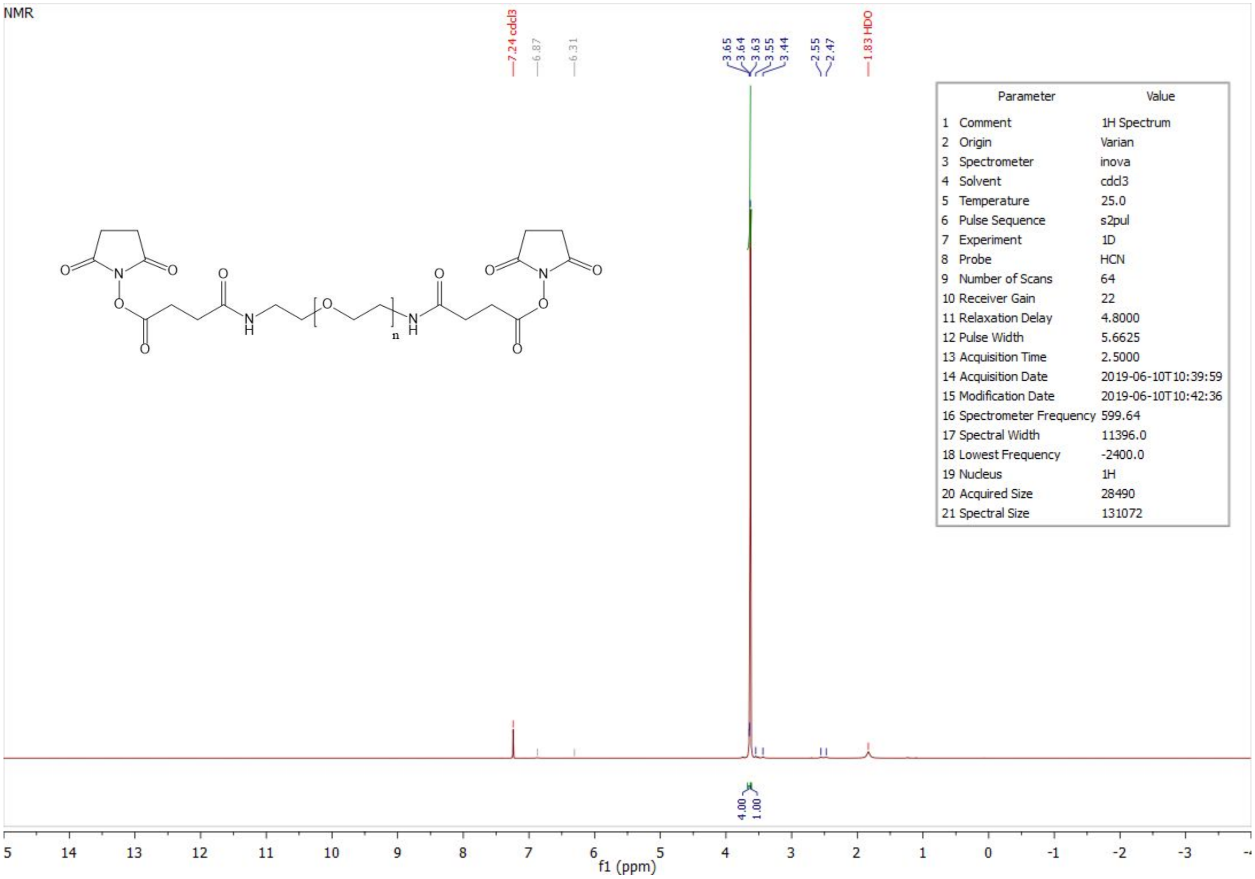

	Parameter	Value
1	Comment	1H Spectrum
2	Origin	Varian
3	Spectrometer	inova
4	Solvent	cdcl3
5	Temperature	25.0
6	Pulse Sequence	s2pul
7	Experiment	1D
8	Probe	HCN
9	Number of Scans	64
10	Receiver Gain	22
11	Relaxation Delay	4.8000
12	Pulse Width	5.6625
13	Acquisition Time	2.5000
14	Acquisition Date	2019-06-10T10:39:59
15	Modification Date	2019-06-10T10:42:36
16	Spectrometer Frequency	599.64
17	Spectral Width	11396.0
18	Lowest Frequency	-2400.0
19	Nucleus	1H
20	Acquired Size	28490
21	Spectral Size	131072

Figure S08: ^{1}H NMR spectrum obtained for PEO 59-mer

Section 2: DEER experimental limitations and analysis

Section 2a: DEER limitations at short distances

There are several fundamental and instrumental limitations of the DEER technique at short (< 2 nm) distances. These limitations are discussed below.

1. Length of the pump pulse. The pump pulse excites a finite bandwidth of spins in the nitroxide spectrum. Throughout the duration of the pulse, different regions of the spectrum will be inverted at different times. If the length of the pump pulse exceeds the period of a dipolar oscillation, the oscillation will be partially averaged out and its corresponding distance will be suppressed in the $P(R_{ee})$. This leads to a loss of information for high frequency dipolar oscillations, which correspond to short distances. On the other hand, because the pump pulses in our experiments are chirp pulses (e.g. linear frequency sweep), increasing the length of the pulse results in more complete inversion and better modulation depth. Therefore, a compromise must be made between less suppression of short distances and higher signal to noise ratio. A detailed theoretical analysis on the effect of shaped pulses on the DEER signal, particularly for longer shaped pulses has not yet been performed and to date there is no general rule or experimental procedure to optimize it[1]. Typically, pulse durations shorter than a quarter of the principal dipolar evolution period are sufficient. For the experiments in this study, pump pulse lengths of 100 ns were selected. Thus, any dipolar oscillation four times this (400 ns) are observable. This corresponds to a frequency of 2.5 MHz and a rough distance of 2.75 nm. We expect that reported distances shorter than this are physical, but partially suppressed, so this limitation is only a rough estimate of the upper limit of dampening issues.

2. Limited pulse bandwidth. The DEER experiment utilizes two resonant microwave frequencies designated for the pump and observe spin populations of the nitroxide EPR spectrum. In the case of large dipolar couplings, the resonance field of the observe spins can be shifted outside the bandwidth of the observe pulses by applying the pump pulse. This is a major issue when the dipolar coupling is similar in magnitude to the bandwidth of the observe pulse. For dipolar coupling frequencies at the limit of the excitation bandwidth, it is possible to apply an excitation bandwidth correction to the kernel function that maps time domain signals from distance distributions. To obtain this correction, the entire pulse sequence must be accounted for in a density matrix simulation. Banham and coworkers applied this method to determine the correction to their analysis, however, this was applied for a DEER with rectangular “hard” pulses at X-band[2]. Our experiments apply shaped pulses at Q-band, thus a full density matrix simulation of the pump and observe pulse sequence averaged over the nitroxide spectrum would be necessary. As a first approximation, we simulated only the observe pulses and assumed the excitation bandwidth of the pump pulse is much greater than the excitation bandwidth of the observe pulses. For a 20 ns $\pi/2$ pulse and 40 ns π pulse, this gives a bandwidth between 12 and 26 MHz for a refocused Hahn echo sequence. This makes the minimum observable distance between 1.3 and 1.6 nm.

3. Breakdown of the assumption of weak dipolar coupling. The calculation of distances through the DEER experiment relies upon the assumption of point dipoles and weak dipolar coupling. Both assumptions begin to break down at short distances (< 1.5 nm)[3,4]. When spin centers approach smaller distances, they begin to experience through-space exchange coupling, which increases the modulation frequency and therefore gives artificially short distances in the DEER signal. This limitation is fundamental and unavoidable in DEER experiments.

4. Sampling rate must exceed Nyquist criterion. For completeness, we mention the requirement that the sampling rate for alias-free signal processing must be twice per oscillation period, formally

called the Nyquist criterion. The experiments in this study were recorded with a sampling rate of 16 ns per point, thus dipolar oscillations with a period of 32 ns or greater are captured. This corresponds to a frequency of 31.25 MHz and a distance of 1.18 nm. This distance is shorter than the limitations imposed by the previous three contributions, thus it is the least significant in DEER data collection and processing.

Section 2b: DEER data analysis

All time domain DEER traces for spin labeled PEO are shown in **Figure 2**. The data was background corrected with a 3D background model and the resulting signal was transformed to a distance distribution, $P(R_{ee})$, by Tikhonov regularization with non-negativity constraint using the LongDistances software by Altenbach[5]. We did not use a parametrized model of the distance distribution (e.g., eqn. (3)) to directly fit the background-corrected DEER data because of uncertainty in the effect of probes and a lack of resolution at short distances. For distance distributions of PEO 5, 13, 25, and 36-mer, a smoothness (or regularization) parameter of 30 was used for the model-free analysis. For the PEO 59-mer a smoothness parameter of 100 was used. This was decided by selecting the highest smoothness parameter that did not add significant additional distortions to the dipolar data fit. The error in $P(R_{ee})$ was estimated using the bootstrapping method available in the LongDistances software. The transformation applies a Tikhonov regularization to solve the ill-posed mathematical problem $V = KP$ where V is the dipolar signal in the time domain, P is the distance distribution, and K is the kernel matrix relating them.[6,7] There exist other methods for solving this problem, including maximum entropy regularization[6], global Gaussian-based model fitting[8], Srivastava–Freed Truncated Singular Value Decomposition (SF-TSVD),[9,10] the use of Bayesian statistical inversion approaches to determine uncertainty in $P(R_{ee})$,[11] as well as most recently, a global parameter-free distribution approach by DEERLab[12]. However, the Tikhonov regularization is the most widely used DEER data analysis approach to solve the inversion problem, and for data as presented here acquired with sufficiently long dipolar evolution time and high signal to noise ratio, a robust approach. Of note, the shape of $P(R_{ee})$ is distinctly non-Gaussian and does not obey any analytical functional form, reflective of the polymer physical property of PEO of various length as presented in this study, and hence some of the alternate approaches to finding solutions to $P(R_{ee})$ are less than ideal. However, e.g. SF-TSVD and DEERLab will readily yield the same solutions for $P(R_{ee})$ as Tikhonov regularization for data at hand in this study.

Section 3: The GaFF2 force-field and 4-site OPC water model

The input structure to Gaussian '16 was generated using Avogadro and initially energy-minimized using the GAFF2 force field.[13–15] The input structure then underwent a geometry optimization in Gaussian before the electrostatic potential (ESP) around the molecule was output. The discretized ESP was then used to perform RESP charge fitting using the antechamber software which is distributed with the AmberTools 2016 package.[16–18] To further investigate the effect of charging on the results, we also obtained a separate set of partial charges for the PEO monomers (no TEMPO groups) using the empirical AM1-BCC charge fitting procedure in antechamber.[19,20]

Section 3a: Charging the unlabeled PEO polymer

Charging for the unlabeled PEO was conducted by trying a series of PEO oligomers (1,3,5,7 and 9-mers) to assess how the charging on the center monomer evolved with chain length, **Figure S09** right. It was observed that the charges on the central monomer plateaued by the 5-mer, **Figure S10**. Given that we did not consider varying confirmations effect on the charges (i.e. we only considered linear PEO chains), we believed any further refinement from going beyond the 5-mer would be insignificant as compared to changes from conformational effects (and/or solvation effects). Several different quantum calculations were conducted to assess how much the charges depended on the type of calculation, **Figure S09 left**; we chose to stick with the B3LYP/6-311++G** functional/basis set as prior work found this to produce good results for PEO in the melt.[21] Our charging results also yielded very similar RESP charges to theirs, **Figure S10** open symbols.

Index	Charging	ESP Mesh	O	C	H
1	AM1-BCC		-0.4296	0.1294	0.0427
2	B3LYP 6-311++G**	rings = 4 pts./A^2=1	-0.5400	0.2280	0.0210
2	B3LYP 6-311++G** SCRF=water	rings = 4 pts./A^2=1	-0.65718	0.26651	0.03028
3	gas/sol. avg.		-0.5986	0.2473	0.02864
4	B3LYP 6-311++G**	rings = 7 pts./A^2=8	-0.717796	0.447166	-0.044134
5	B3LYP 6-311++G** SCRF=water	rings = 7 pts./A^2=8	-0.773895	0.456456	-0.036097
6	gas/sol. avg.		-0.74585	0.45181	-0.04011
7	HF/6-31G*	rings = 4 pts./A^2=1	-0.466552	0.163223	0.034690
8	HF/6-31G* SCRF=water	rings = 4 pts./A^2=1	-0.678291	0.242797	0.045890
9	gas/sol. avg.		-0.57242	0.20301	0.04029
10	TraPPe-FF		- 0.50	0.25	N/A

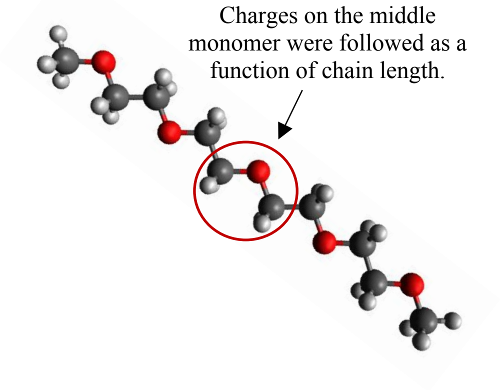

Charges on the middle monomer were followed as a function of chain length.

Figure S09: (**left**) The sensitivity of the fixed charges to the level of theory (first column) used to get the electrostatic potential around the molecule. The B3LYP/6-311++G** was conducted for two different sets of rings and points per angstrom^2 on the surface of these rings; the results were seen to vary significantly between the two. The AM1-BCC charging gave similar charges to the HF/6-31G* calculation followed by RESP fitting, as would be expected as the semi-empirical AM1-BCC approach is designed to reproduce HF/6-31G* the electrostatic potential (ESP) around the molecule. The results in this paper used the B3LYP results for 7 rings around the molecule with a point density of 8 per angstrom^2. These results are for a 5-mer (the charges have already converged at this length) tracking the charges on the center monomer. Also shown are the charges if using a self-consistent reaction field (SCRF with PCM and water as the solvent) approach to account for the solvent environment. In all cases, the inclusion of the solvent increased the polarization of the bonds in the molecule. (**right**) Image of the 5-mer and the central monomer that was followed for deriving charges on the polymer.

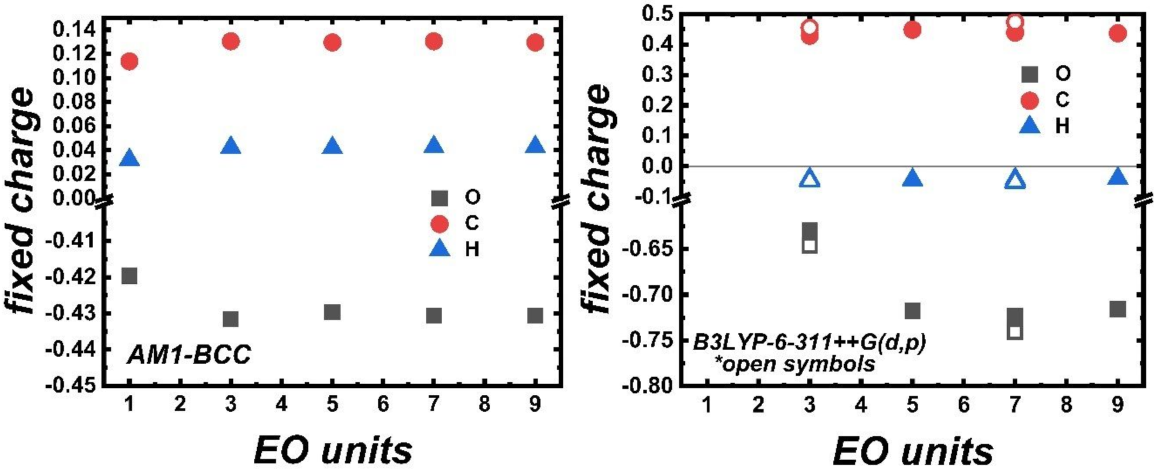

Figure S10: Convergence of the middle monomer fixed charged with chain length. (**left**) The AM1 charging scheme. (**right**) The B3LYP/6-311++G** functional and basis set were used for gas-phase calculations, followed by RESP fitting using the antechamber package. *Open symbols are from the work of Barbosa, *et al.*[21]

Since it is not practical to run quantum calculations on high molecular weight polymers, the charging scheme implemented here ran charging calculations on 5-mers and took the middle monomer set of charges. In the case of AM1-BCC charging, the whole polymer (including the two monomers on the ends, as the ends were not drastically different than the middle) received the middle charge; the values of the charges were slightly changed (order ~0.001) to ensure the monomer charges were neutral. In the case of the B3LYP charging scheme again the middle monomer RESP charges were used for the entire chain, except here, the two end monomers were not changed from the ends of the 5-mer. The charges used for the middle monomers are presented above in **Figure S09 left** and the values for the smaller PEO oligomers, below in **Figure S11**.

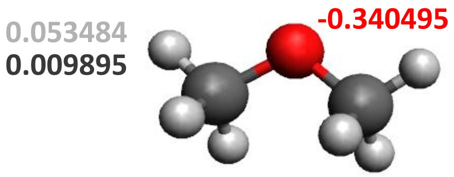
0.053484
0.009895
-0.340495

PEO 1-mer

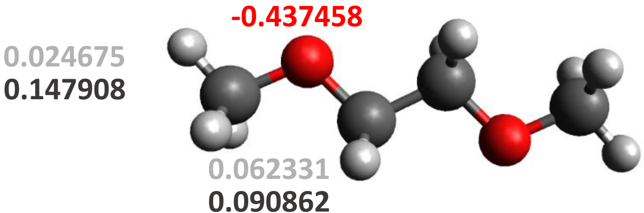
-0.437458
0.024675
0.147908
0.062331
0.090862

PEO 2-mer

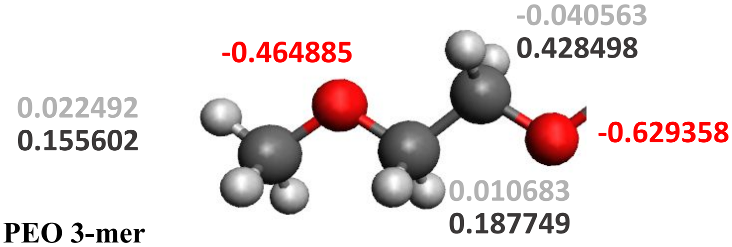
-0.040563
0.428498
-0.464885
0.022492
0.155602
-0.629358
0.010683
0.187749

Left half, PEO 3-mer

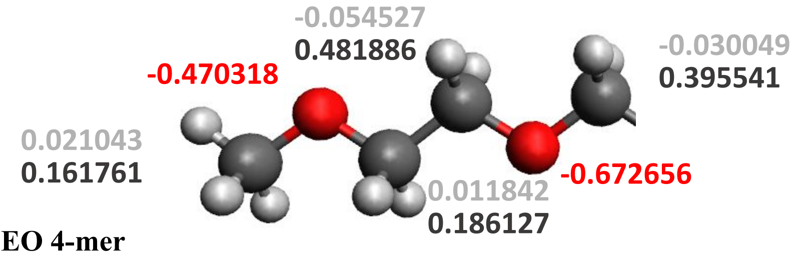
-0.054527
0.481886
-0.030049
0.395541
-0.470318
0.021043
0.161761
-0.672656
0.011842
0.186127

Left half, PEO 4-mer

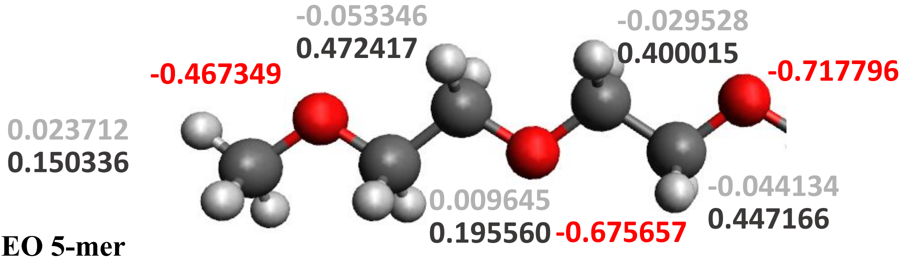
-0.053346
0.472417
-0.029528
0.400015
-0.467349
-0.717796
0.023712
0.150336
-0.044134
0.447166
0.009645
0.195560
-0.675657

Left half, PEO 5-mer

Figure S11: Charges for the PEO oligomers from the B3LYP charging. The charges are symmetric around the molecule. The charges on the two end monomers for the 5-mer were kept on the longer PEO chains, while the middle monomer charges were fixed to the value reported in **Figure S09 left.**

Section 3b: Charging the spin probe labeled PEO

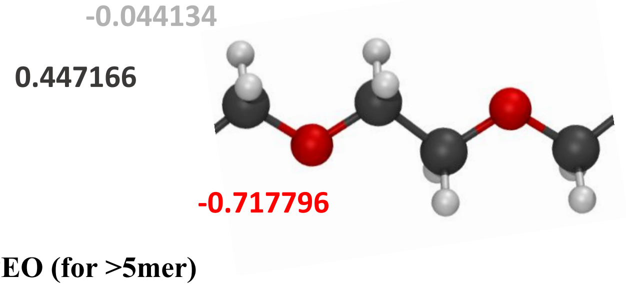
-0.044134
0.447166
-0.717796

PEO (for >5mer)

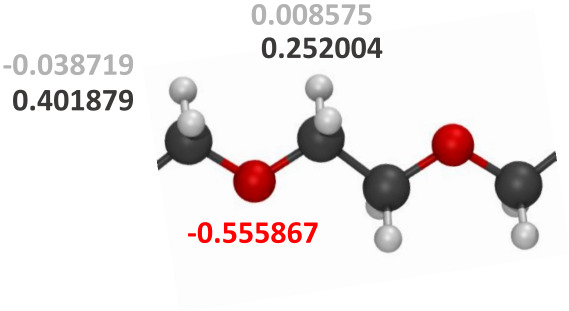
0.008575
0.252004
-0.038719
0.401879
-0.555867

PEO 2-mer

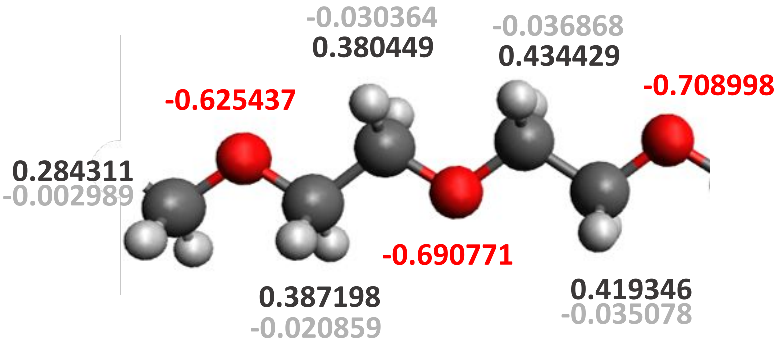
-0.030364
0.380449
-0.036868
0.434429
-0.625437
-0.708998
0.284311
-0.002989
-0.690771
0.387198
-0.020859
0.419346
-0.035078

Left Half, PEO 5-mer

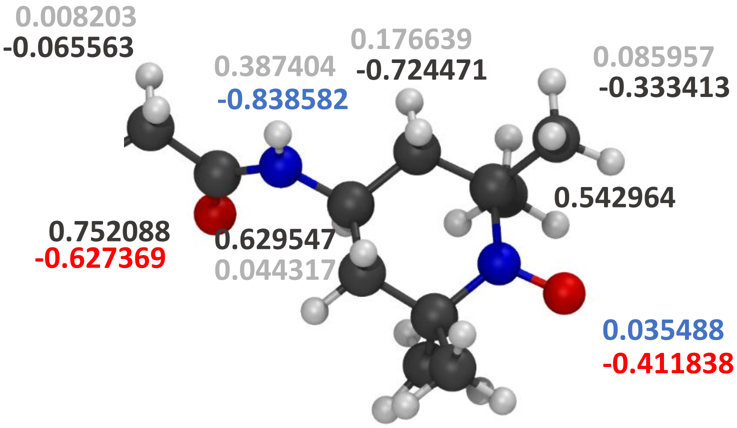
0.008203
-0.065563
0.387404
-0.838582
0.176639
-0.724471
0.085957
-0.333413
0.542964
0.752088
-0.627369
0.629547
0.044317
0.035488
-0.411838

Short Linker + 4-Amino TEMPO, PEO 2-mer

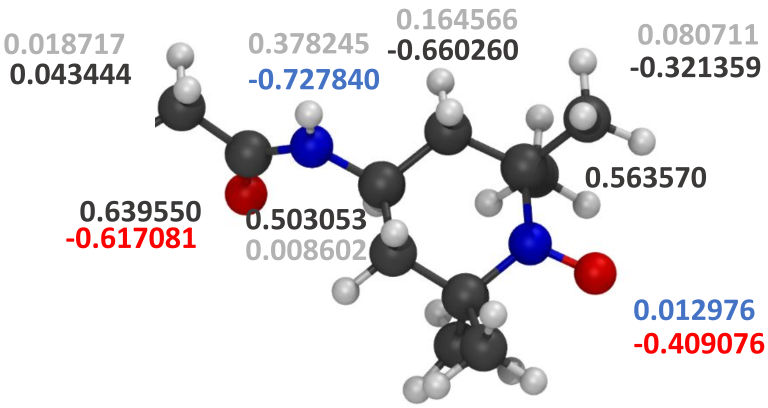
0.018717
0.043444
0.378245
-0.727840
0.164566
-0.660260
0.080711
-0.321359
0.563570
0.639550
-0.617081
0.503053
0.008602
0.012976
-0.409076

Short Linker + 4-Amino TEMPO, PEO 5-mer

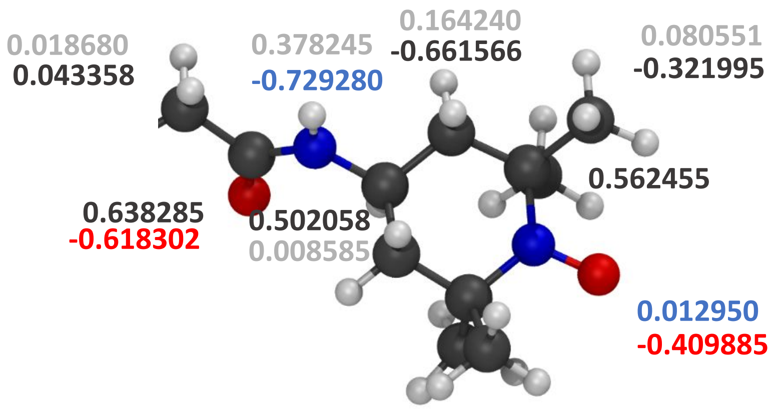
0.018680
0.043358
0.378245
-0.729280
0.164240
-0.661566
0.080551
-0.321995
0.562455
0.638285
-0.618302
0.502058
0.008585
0.012950
-0.409885

Short Linker + 4-Amino TEMPO, PEO 13-mer and 25-mer

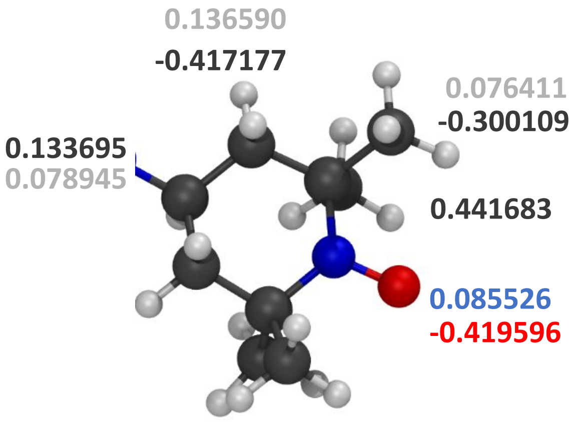
0.136590
-0.417177
0.076411
-0.300109
0.133695
0.078945
0.441683
0.085526
-0.419596

4-Amino TEMPO, PEO 36-mer and 59-mer

Figure S12: Charges for the PEO oligomers (between two TEMPO probes) from the B3LYP charging. The charges are symmetric around the molecule. For the 13-mer, 25-mer, 36-mer and 59-mer, the monomer charges were fixed to the value reported in **Figure S09 left.**

Section 3c: PEO solution densities

Below are the solution densities for a PEO 5mer across temperature and composition. Solution densities are one metric in analyzing the reliability of a force-field. We are considering in this work dilute PEO solutions, which is where the density data below agree well with experiment. However, as the PEO chain mole fraction increases, an increasing discrepancy between the experimental densities occurs. Importantly, at all charging schemes capture the temperature trend qualitatively and the two B3LYP charging schemes retain a pronounced maximum in the density profiles in reasonable agreement with the experimental data.

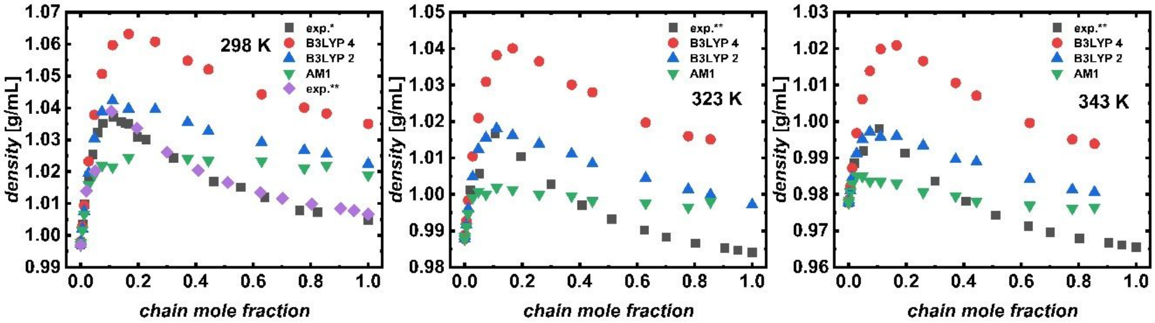

Figure S13: Density (g/mL) of PEO 5-mer aqueous solutions (OPC water model) at three different temperatures, 298 (**left**), 323 (**center**) and 343K (**right**) at 1 atm. Two different sets of experimental data were taken from the literature for 298K, while there was only one set for 323 and 343K.[22,23]

Section 4: Molecular dynamics simulation protocol

This section includes details for the molecular dynamics (MD) simulation protocol used. First, we needed to decide on the number of solvent molecules to add to ensure the polymers were well into the dilute regime. This was determined by using the empirical relationship between R_g and molecular weight from Devanand and Selser[24]:

$$R_g = 0.0222 \times MW[Da]^{0.5791}[=]nm's.$$

This gives an estimate for the size of the polymer, from which the overlap segment concentration can be estimated:

$$\varphi^* = \frac{EO\ length}{4\pi R_g^3}[=]monomers/volume.$$

The minimum box volume can now be determined as follows:

$$V_{box}^{min} = \ EO\frac{length}{\varphi^*}[=]nm^3.$$

At this point, to ensure that the simulations are below φ^* a "fudge factor" of 0.05 was chosen, thus the box volume would be: $V_{box} = V_{box}^{min}/0.05$. The corresponding box side length would then be:

$$L_{box} = V_{box}^{1/3}[=]nm's.$$

For the shortest polymers the L_{box} lengths go below the cutoff for the pair potentials, $r_{cut} = 1.0$ nm's; thus, a minimum L_{box} was chosen to be well above this (i.e. 3 nm's for 1-mer and 5 nm's for 2 through 9-mers). The number of waters required to get close to this volume were then determined from the density of water at room temperature and pressure (a dilute PEO molecule does not change the density significantly).

The atomic coordinates were output every 10 picoseconds (ps) to ensure that the output frequency was below the correlation times for even the shortest PEO oligomers. While the output frequency could have been decreased for larger chains, we held it fixed throughout. Depending on the chain size, the annealing time was chosen loosely based on initial estimates for the end-to-end correlation times, see **SI Section 07** for details. The NVT annealing was then followed by an NPT cooldown and then a box-sizing run to get the average box volume. Then the production run was started from an NPT frame from the box sizing equilibration step that was within 0.001 of the average volume.

All thermodynamic and structural property averages were calculated using a custom Python statistics script to ensure samples were decorrelated; the results were also checked against the timeseries module of pymbar which yielded very similar results.

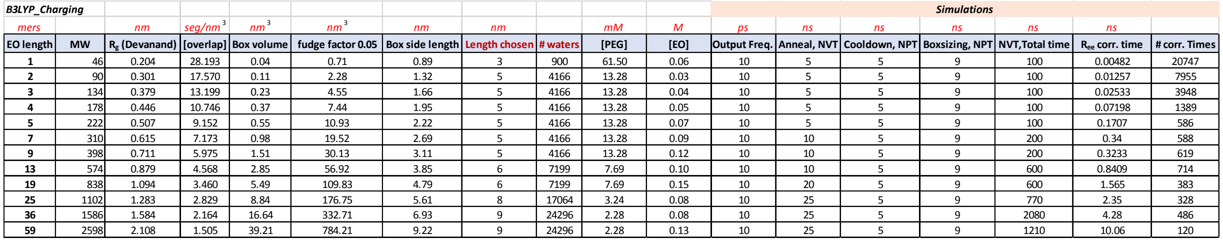

B3LYP_Charging											*Simulations*						
mers		nm	seg/nm^3	nm^3	nm^3	nm	nm		mM	M	ps	ns	ns	ns	ns	ns	
EO length	MW	R_g (Devanand)	[overlap]	Box volume	fudge factor 0.05	Box side length	Length chosen	# waters	[PEG]	[EO]	Output Freq.	Anneal, NVT	Cooldown, NPT	Boxsizing, NPT	NVT,Total time	R_{ee} corr. time	# corr. Times
1	46	0.204	28.193	0.04	0.71	0.89	3	900	61.50	0.06	10	5	5	9	100	0.00482	20747
2	90	0.301	17.570	0.11	2.28	1.32	5	4166	13.28	0.03	10	5	5	9	100	0.01257	7955
3	134	0.379	13.199	0.23	4.55	1.66	5	4166	13.28	0.04	10	5	5	9	100	0.02533	3948
4	178	0.446	10.746	0.37	7.44	1.95	5	4166	13.28	0.05	10	5	5	9	100	0.07198	1389
5	222	0.507	9.152	0.55	10.93	2.22	5	4166	13.28	0.07	10	5	5	9	100	0.1707	586
7	310	0.615	7.173	0.98	19.52	2.69	5	4166	13.28	0.09	10	10	5	9	200	0.34	588
9	398	0.711	5.975	1.51	30.13	3.11	5	4166	13.28	0.12	10	10	5	9	200	0.3233	619
13	574	0.879	4.568	2.85	56.92	3.85	6	7199	7.69	0.10	10	10	5	9	600	0.8409	714
19	838	1.094	3.460	5.49	109.83	4.79	6	7199	7.69	0.15	10	20	5	9	600	1.565	383
25	1102	1.283	2.829	8.84	176.75	5.61	8	17064	3.24	0.08	10	25	5	9	770	2.35	328
36	1586	1.584	2.164	16.64	332.71	6.93	9	24296	2.28	0.08	10	25	5	9	2080	4.28	486
59	2598	2.108	1.505	39.21	784.21	9.22	9	24296	2.28	0.13	10	25	5	9	1210	10.06	120

Table S02: How an initial box size was picked to ensure the polymers were in the dilute regime and the simulation times for the various equilibration and production runs. For the B3LYP charged polymers.

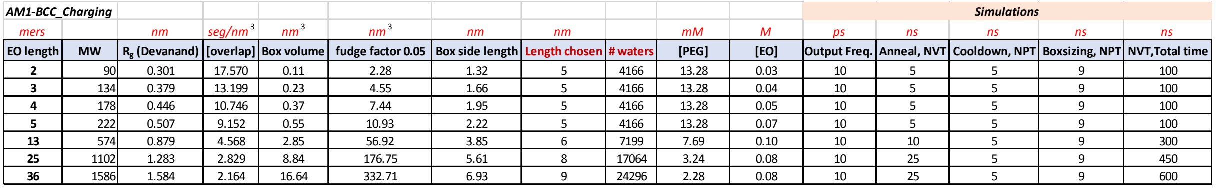

AM1-BCC_Charging										*Simulations*				
mers		*nm*	*seg/nm^3*	*nm^3*	*nm^3*	*nm*	*nm*		*mM*	*M*	*ps*	*ns*	*ns*	*ns*	*ns*
EO length	**MW**	**R_g (Devanand)**	**[overlap]**	**Box volume**	**fudge factor 0.05**	**Box side length**	**Length chosen**	**# waters**	**[PEG]**	**[EO]**	**Output Freq.**	**Anneal, NVT**	**Cooldown, NPT**	**Boxsizing, NPT**	**NVT,Total time**
2	90	0.301	17.570	0.11	2.28	1.32	5	4166	13.28	0.03	10	5	5	9	100
3	134	0.379	13.199	0.23	4.55	1.66	5	4166	13.28	0.04	10	5	5	9	100
4	178	0.446	10.746	0.37	7.44	1.95	5	4166	13.28	0.05	10	5	5	9	100
5	222	0.507	9.152	0.55	10.93	2.22	5	4166	13.28	0.07	10	5	5	9	100
13	574	0.879	4.568	2.85	56.92	3.85	6	7199	7.69	0.10	10	10	5	9	300
25	1102	1.283	2.829	8.84	176.75	5.61	8	17064	3.24	0.08	10	25	5	9	450
36	1586	1.584	2.164	16.64	332.71	6.93	9	24296	2.28	0.08	10	25	5	9	600

Table S03: How an initial box size was picked to ensure the polymers were in the dilute regime and the simulation times for the various equilibration and production runs. For the AM1-BCC charged polymers.

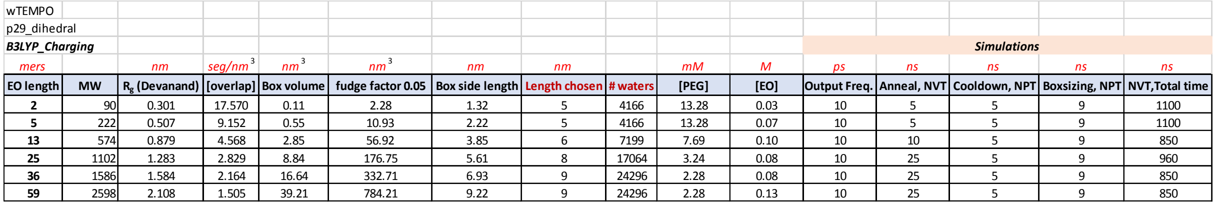

wTEMPO															
p29_dihedral															
B3LYP_Charging											*Simulations*				
mers		*nm*	*seg/nm^3*	*nm^3*	*nm^3*	*nm*	*nm*		*mM*	*M*	*ps*	*ns*	*ns*	*ns*	*ns*
EO length	**MW**	**R_g (Devanand)**	**[overlap]**	**Box volume**	**fudge factor 0.05**	**Box side length**	**Length chosen**	**# waters**	**[PEG]**	**[EO]**	**Output Freq.**	**Anneal, NVT**	**Cooldown, NPT**	**Boxsizing, NPT**	**NVT,Total time**
2	90	0.301	17.570	0.11	2.28	1.32	5	4166	13.28	0.03	10	5	5	9	1100
5	222	0.507	9.152	0.55	10.93	2.22	5	4166	13.28	0.07	10	5	5	9	1100
13	574	0.879	4.568	2.85	56.92	3.85	6	7199	7.69	0.10	10	10	5	9	850
25	1102	1.283	2.829	8.84	176.75	5.61	8	17064	3.24	0.08	10	25	5	9	960
36	1586	1.584	2.164	16.64	332.71	6.93	9	24296	2.28	0.08	10	25	5	9	850
59	2598	2.108	1.505	39.21	784.21	9.22	9	24296	2.28	0.13	10	25	5	9	850

Table S04: How an initial box size was picked to ensure the polymers were in the dilute regime and the simulation times for the various equilibration and production runs. For the B3LYP charged polymers with spin labels.

Section 5: Convergence of labeled to unlabeled PEO $\tilde{R}_{ee}$ values

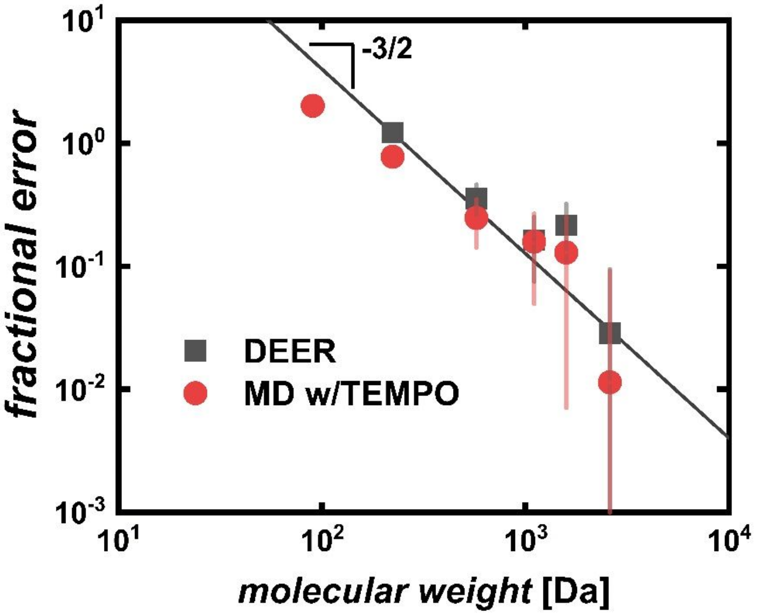

Figure S14: The rate of convergence of spin labeled PEO to unlabeled values as captured by the fractional error between MD without spin labels, $\tilde{R}_{ee}$, to both labeled, $\tilde{R}_{ee}^{TEMPO}$, DEER measurements and MD simulations. Fractional error defined as: $(\tilde{R}_{ee}^{TEMPO} - \tilde{R}_{ee})/\tilde{R}_{ee}$. The convergence appears to agree with the prediction by Jacobson-Stockmayer (JS) theory ($\sim MW^{-3/2}$, JS scaling for Gaussian chain light grey line), though would be expected to converge quicker for excluded volume chains. In this work, due to experimental constraints, the largest to TEMPO labeled chains (the 36- and 59-mers) have linkers that are longer, which leads to the blip in both the MD w/TEMPO and DEER data most notable at the 36-mer (1600 Da). Error bars are ± 1 standard error.

The exponent for excluded volume chains, τ, is expected to be larger than the $3/2$, since excluded volume interactions further penalize closer separations decreasing the probability of short separations.

Section 6: Spin-probe Aggregation

Comparison between the P_{ee}'s from the spin labeled and unlabeled MD simulations. The R_{ee}'s were calculated from the last carbon of the PEO chains for both the labeled and unlabeled simulations, not from the TEMPO radical.

$$\ln\left(\frac{P_{ee}^{unlabeled}}{P_{ee}^{labeled}}\right) = -\beta U_{unlabeled} + \beta U_{labeled} + constant$$

$$\ln\left(\frac{P_{ee}^{unlabeled}}{P_{ee}^{labeled}}\right) = \Delta\beta U + constant$$

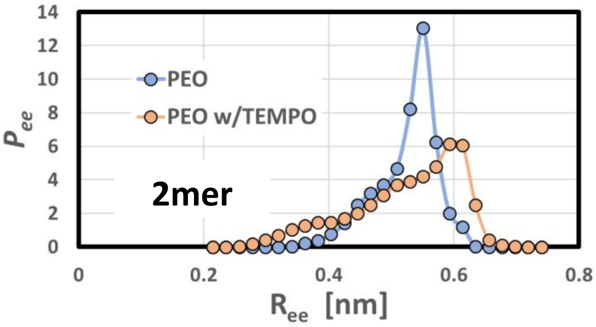

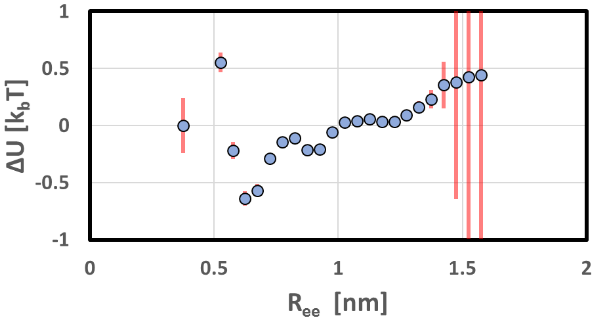

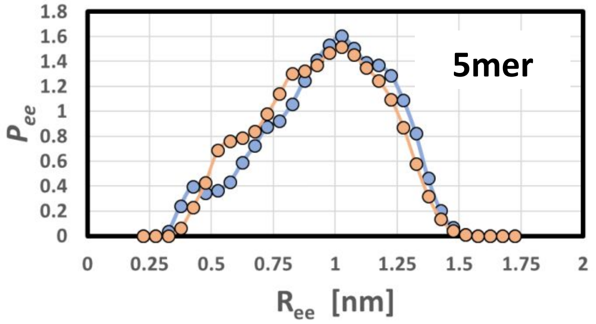

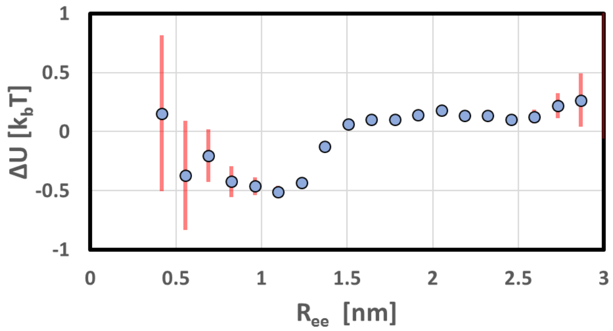

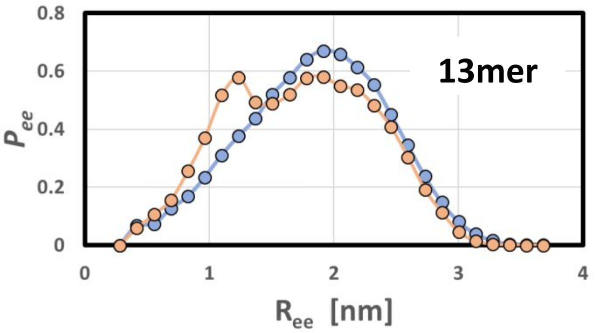

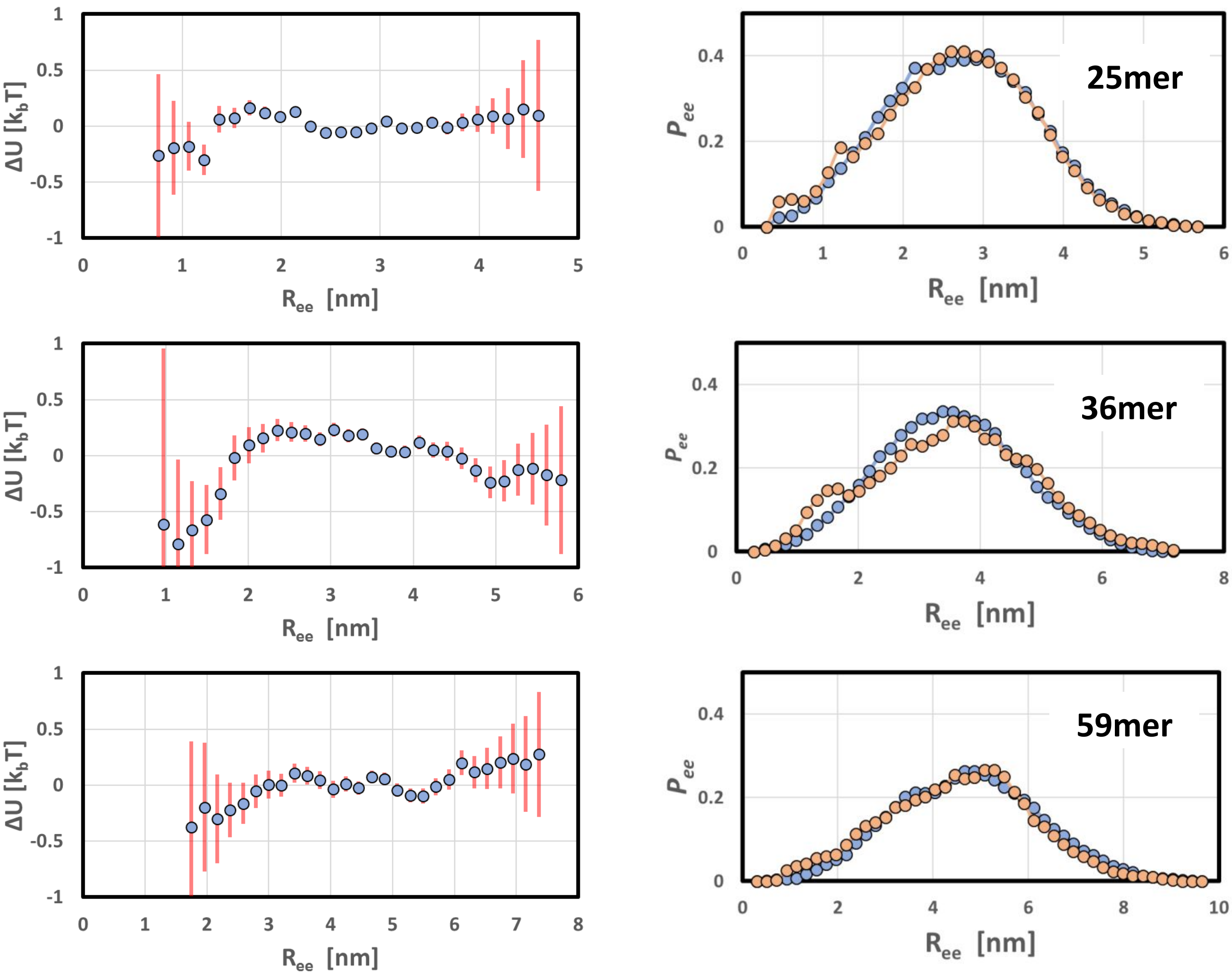

Figure S15: The ΔU, left panels, between the unlabeled and labeled chains calculated from the logarithm of the ratio of the P_{ee}'s, right panels. The data is for the 2, 5, 13, 25, 36 and 59mer in descending order. The aggregation energy scale is roughly consistent between all chains with a depth on the order of $\sim 0.7 k_b T$. The error bars are +/- 1 std. dev.

Section 7:

Section 7a: $\tilde{R}_{ee}$ average values compared to other literature models

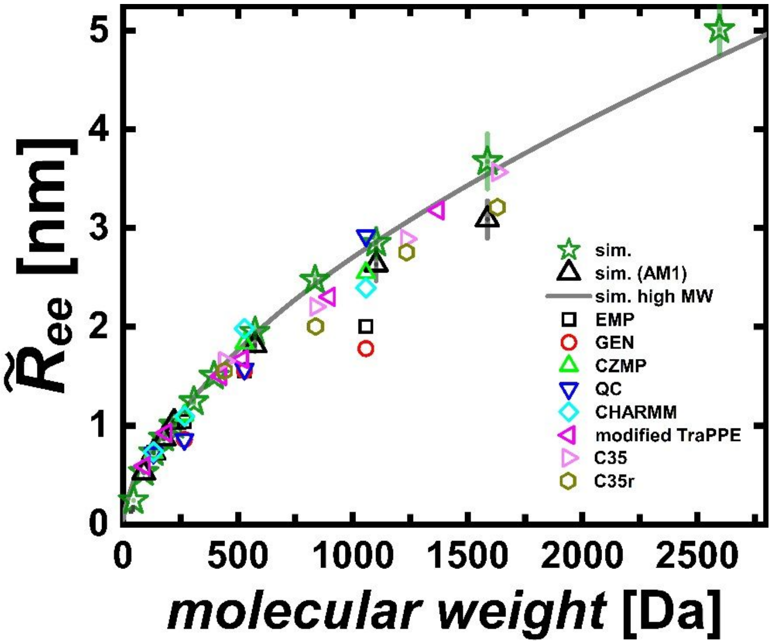

Figure S16: $\tilde{R}_{ee}$ values from this work compared to a variety of proposed PEO models in the literature.[25–27] The PEO model used in this work – with B3LYP charging, not AM1 – compares structurally quite favorably to the other models, though the modified-TraPPE (Fischer *et al.* reparametrized the original dihedral potential to new ab-initio data)[25] force-field does a good job as well.

Section 7b: $\tilde{R}_{ee}$ and $\tilde{R}_g$ data from scattering experiments

Index	MW	Rg	Ree	Source	Method
1	173000	22.1	55.17	A	LS
2	348000	32.6	81.39	A	LS
3	538000	41.4	103.38	A	LS
4	611000	50.2	125.50	A	LS
5	868000	53.0	132.52	A	LS
6	882000	56.6	141.42	A	LS
7	2260000	96.3	240.70	A	LS
8	4460000	150.3	375.83	A	LS
9	11000000	380.8	951.97	A	LS
10	252000	30.4	76.00	B	LS
11	570000	50.8	127.00	B	LS
12	594000	48.3	120.75	B	LS
13	838000	59.4	148.50	B	LS
14	860000	61.5	153.75	B	LS
15	996000	69.8	174.50	B	LS
16	25000	6.5	16.25	C	LS
17	40000	10.0	25.00	C	LS
18	73000	13.5	33.75	C	LS
19	150000	19.1	47.75	C	LS
20	280000	29.4	73.50	C	LS
21	660000	45.5	113.75	C	LS
22	1290000	63.6	159.00	C	LS
23	16000	5.4	13.50	D	N
24	35000	7.3	18.25	D	N
25	10000	4.0	10.00	D	N
26	20000	6.1	15.25	D	N
27	30000	7.5	18.75	D	N
28	167000	23.0	57.50	E	LS
29	216000	26.0	65.00	E	LS
30	331000	28.0	70.00	E	LS
31	497000	37.0	92.50	E	LS
32	572000	41.0	102.50	E	LS
33	21000	4.6	11.5	F	N
34	153000	20.0	50.0	F	N
35	248000	14.8	37.0	F	N
36	2000	1.4	3.4	G	N
37	4000	2.2	5.4	G	N
38	8000	2.6	6.5	G	N
39	5000	3.1	7.8	D	N
40	400	0.6	1.5	H*	N
41	1000	0.9	2.1	H*	N
42	1560	1.6	4.0	F	N
43	3000	2.20	5.5	I	N
44	5000	2.42	6.1	I	N

Table S05: $\tilde{R}_g$ values compiled from the literature measured using either light (LS) or neutron (N) scattering. The corresponding $\tilde{R}_{ee}$ values were calculated from $\tilde{R}_g$ using the relation the asymptotically valid, excluded volume relation: $\tilde{R}_{ee} = 2.5\tilde{R}_g$. The data above a molecular weight of 10kDa ($n = 35$) was collective fit to the asymptotic power law relation: $\tilde{R}_g = a(MW)^{\nu}$. The exponent was fixed to 0.588, corresponding to the excluded volume regime, and the chemistry dependent pre-factor was fit to the data, $a = 0.047(4)/\sqrt{6.25}$. An excellent fit was achieved – see solid, grey line of **Figure 4** in the main text. Sources are (Temperature): A[28] (25C), B[24] (30C), C[29] (25C), D[30] (25C), E[31] (25C), F[32] (60C), G[33] (22C), H[34,35](37C), I[36]. (*)R_g values were averaged from the two papers associated with source H, entries 40 and 41.

Section 7c: R_{ee} Correlation Times

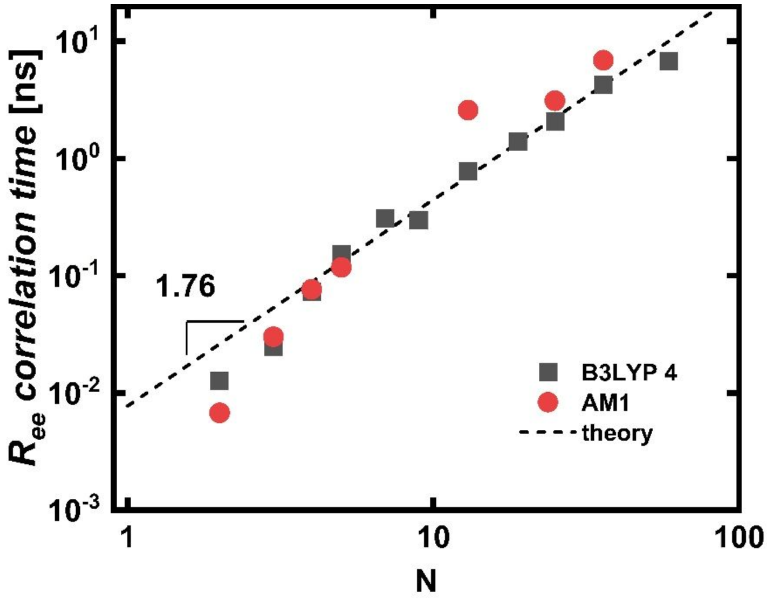

Figure S17: The end-to-end correlation times from the unlabeled PEO, MD simulations. Both the B3LYP 4 and AM1 charged chains' R_{ee} correlation times crossover to Zimm scaling with increasing molecular weight.[37] The 59mer, the longest chain studied, had ~ 100 R_{ee} correlation times.

Section 8: $\tilde{R}_g$ values

Section 8a: $\tilde{R}_g$ values compared to light scattering data

While the DEER spectroscopy technique measures P_{ee} directly and subsequently any higher moments of the distribution (i.e. ensembled average $\tilde{R}_{ee}$), traditional scattering techniques measure $\tilde{R}_g$ (pursuant a scattering model). To compare literature $\tilde{R}_g$ values to our $\tilde{R}_{ee}$ values, we used the asymptotic relation between $\tilde{R}_{ee}$ and $\tilde{R}_g$: $\tilde{R}_{ee}^2 = 6.25\tilde{R}_g^2$ (the pre-factor of 6.25 is for an excluded volume chain, the proportionality factor for a Gaussian chain is 6). We present $\tilde{R}_g$ vs. molecular weight results for the simulations used in this work below; here again, agreement is not only qualitative, but quantitative in the case of the B3LYP charged polymer once the excluded volume regime is reached (i.e. once the polymer grows beyond its thermal blob size).

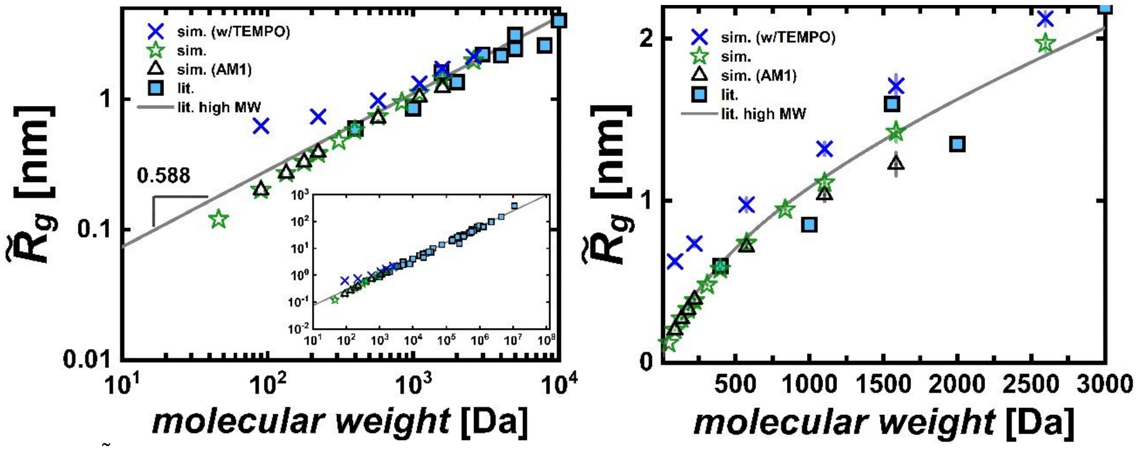

Figure S18: $\tilde{R}_g$ scaling from MD simulations compared to prior literature data from various scattering experiments (light and neutron), sources in **SI Section 6b**. Note the crossover to excluded volume scaling: $\tilde{R}_g \sim MW^{0.588}$. The solid, grey line is a power-law fit to the relation for excluded volume scaling, $\tilde{R}_g = aMW^v$, where the exponent was fixed to the best available prediction, $v \sim 0.588$, while the pre-factor, a, was fit to the compiled $\tilde{R}_g$ values from the literature from high-molecular weight ($> 10\ kDa$) scattering experiments (sample size, $n = 35$). **Left.** Log-log plot of the $\tilde{R}_g$ averages covering the entire range of available data; until now, there has been a considerable lack of reliable data in the low-molecular weight regime ($< 3000\ kDa$). **Right.** Linear plot of the data focusing in on the low-molecular weight regime, simulations of the labeled and unlabeled PEO chains begin to overlap as the molecular weight of the polymer grows. Simulation results for assigning fixed-charges using the a semi-empirical, quantum calculation, AM1-BCC (AM1), are also shown, black triangles. +/- 1 standard error is shown for the $\tilde{R}_g$ simulation values.

Section 8b: $\tilde{R}_g$ values compared to other PEO literature models

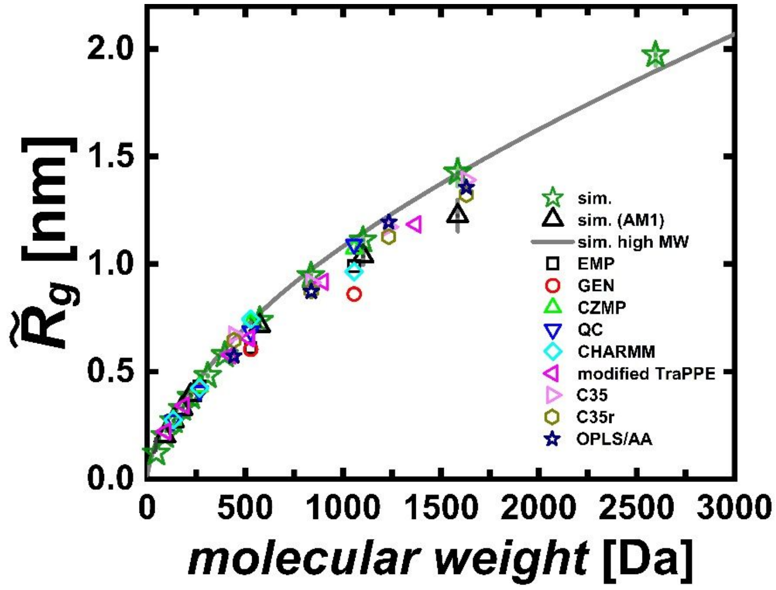

Figure S19: $\tilde{R}_g$ values from this work compared to a variety of proposed PEO models in the literature.[25–27,38] The PEO model used in this work – B3LYP charging – compares structurally quite favorably with the existing experimental data. The AM1 charged model and most of the other force-fields, even the modified-TraPPE force field, seem to be underpredicting $\tilde{R}_g$.

Section 9: R_{ee} vs. molecular weight fits

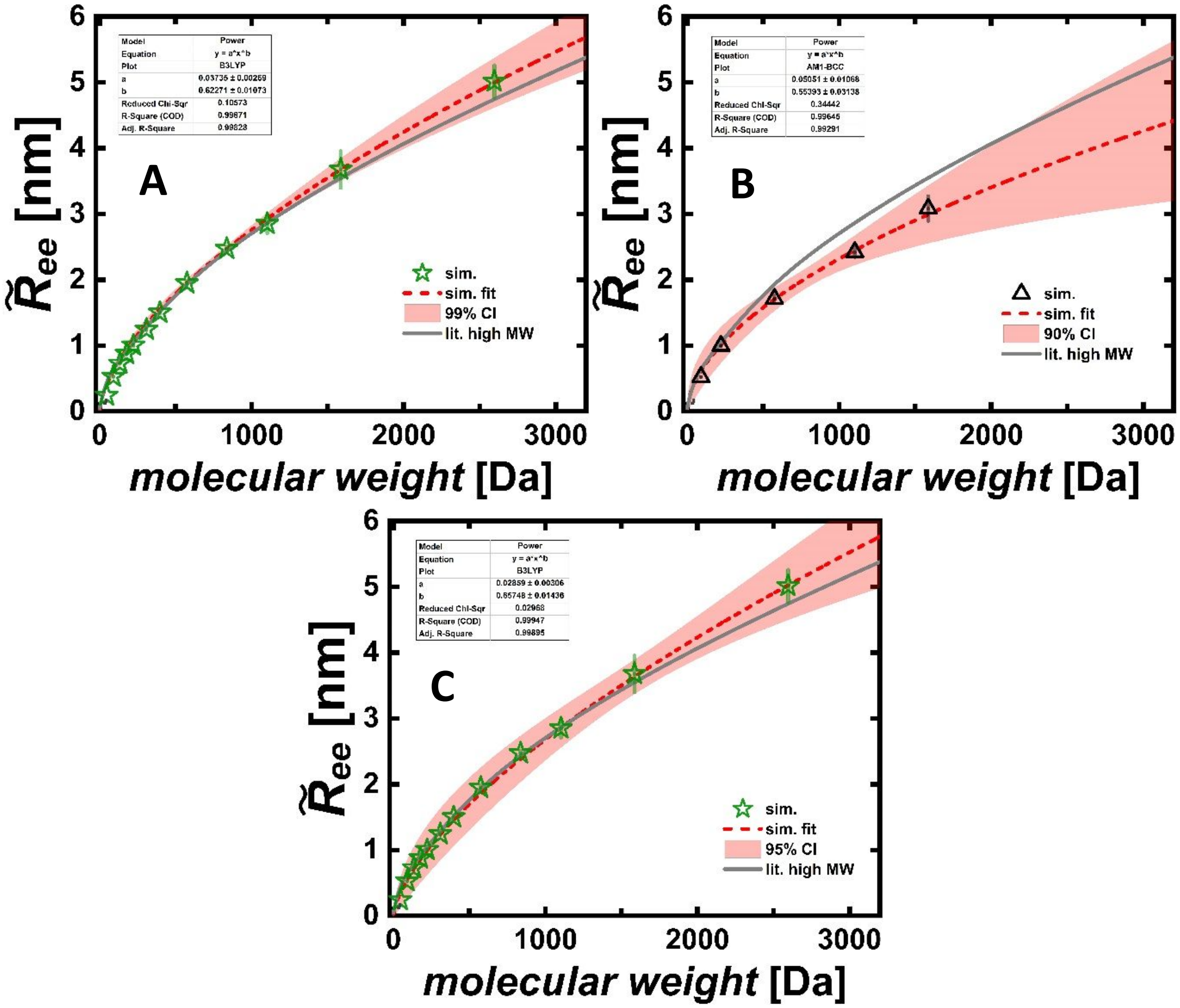

Figure S20: $\tilde{R}_{ee}$ values from this work fit to the functional form: $\tilde{R}_{ee} = aMW^{v}$ using least-squares regression with instrumental error weighting of the fit data: $1/\sigma_i^2$ where σ_i^2 is the error associated with the data point; both the chemistry and solvent dependent parameters were allowed to float during fitting. **(A)** Fit of the B3LYP-4 charged model for chains at or above a MW 574 Da ($n = 5$), $v = 0.62 \pm 0.01$. **(B)** Fit of the AM1-BCC charged model for chains at or above a MW 574 Da ($n = 3$), $v = 0.55 \pm 0.03$. **(C)** Refit of the B3LYP-4 charged model for chains at or above a MW 1100 Da ($n = 3$), $v = 0.657 \pm 0.015$. Future studies could extend this work to chains of higher molecular weight to provide increased confidence in the different scaling exponents.

Section 10: PEO persistence length and characteristic ratio from simulation

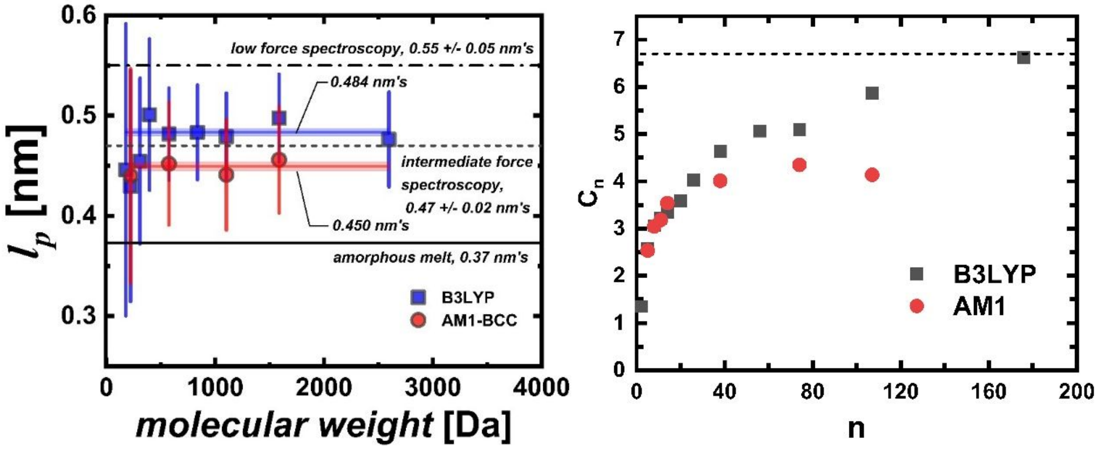

Figure S21: (**Left**) The persistence length of PEO, l_p, calculated from the monomer-monomer bond-vector (between oxygens on the backbone), correlation function. Shaded regions are ± 1 standard error calculated from chains > 500Da; y-bars are ± 1 standard deviation. Results are shown for two different GaFF2 charging schemes, B3LYP 4 and AM1, see **SI Section 3b** for details. Comparison to the available literature data are good. There is some uncertainty for the best estimate of the persistence length due to experimental biases from the force applied, though these single-molecule force spectroscopy measurements are believed to be more accurate than the prior literature value of 0.37 nm's from force-temperature measurements on bulk PEO melts.[37,39,40] (**Right**) The characteristic ratio, $C_n = \langle R_{ee}^2 \rangle / nl^2$, where n is the number of physical bonds and l^2 is the average of the squares of the bond lengths in PEO ($l = 0.147$ nm). The dashed line denotes C_∞ for PEO (6.7),[37] while the online Polymer Properties Database records a composite value of 6.9.

Section 11: Radial distribution functions and water hydration

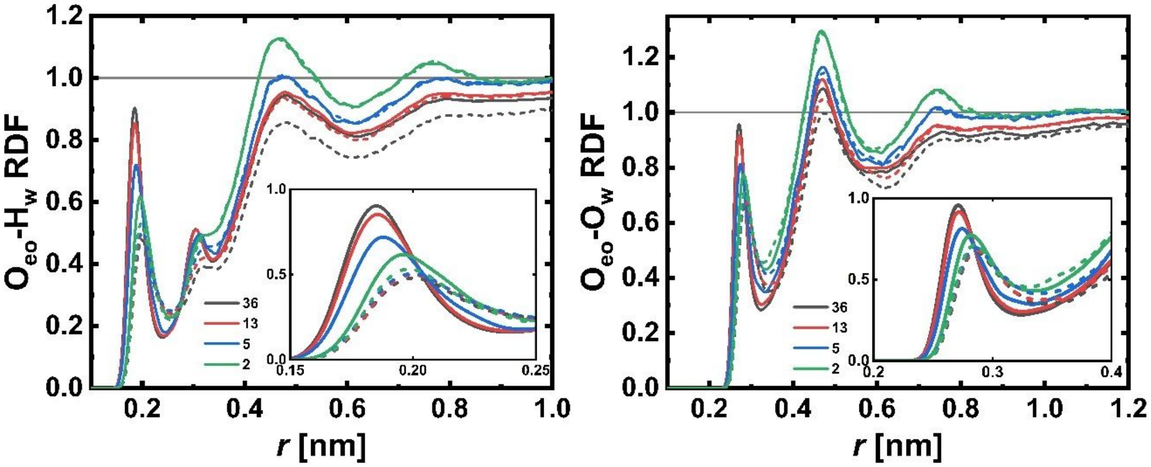

Figure S22: Simulated radial-distribution functions between the oxygen on the PEO backbone, O_{eo}, and the hydrogens on water, H_w (**left**), and water oxygen, O_w (**right**), for the two charge parameterizations of the atomistic force-field, B3LYP 4 solid lines and AM1 dashed lines. The first peak represents strong hydrogen bonding of the water molecules to the ether backbone of PEO and gives rise to PEO's unique water solubility and phase behavior (i.e. LCST and UCST behavior). Interestingly, the degree of hydrogen bonding and qualitative trend of hydrogen bonding with chain length is very sensitive to the charging scheme. In the case of the B3LYP 4, more highly charged oxygen, the hydrogen bonding strengthens with chain length. While for the less high charged, AM1, oxygen, the hydrogen bonding is much weaker and decreases slightly with increasing molecular weight. This is partially attributable to the fact that the B3LYP 4 chains have variably charged end groups, while the AM1 chains are charged the same throughout the chain, see SI Section 2. The end effect for the B3LYP 4 chains decreases with increasing chain length. However, there may still be some additional increased hydrogen bonding for increasing chain length, due to the increasing conformational landscape of the polymer chain that could assume conformations more suited to hydrogen bonding with water.

The signature of a weaker hydrogen bond with the AM1 charges is readily seen in the intensities of the ether-water radial distributions functions (RDF), with the first peak in the $O_{eo} - H_w$ RDF decreasing nearly two-fold, see **SI Section 11**. The poorer solvent quality for the less polar, AM1 PEO is reflected in a smaller, fitted scaling exponent: $\nu = 0.55 \pm 0.03$, **Figure S20 B**.

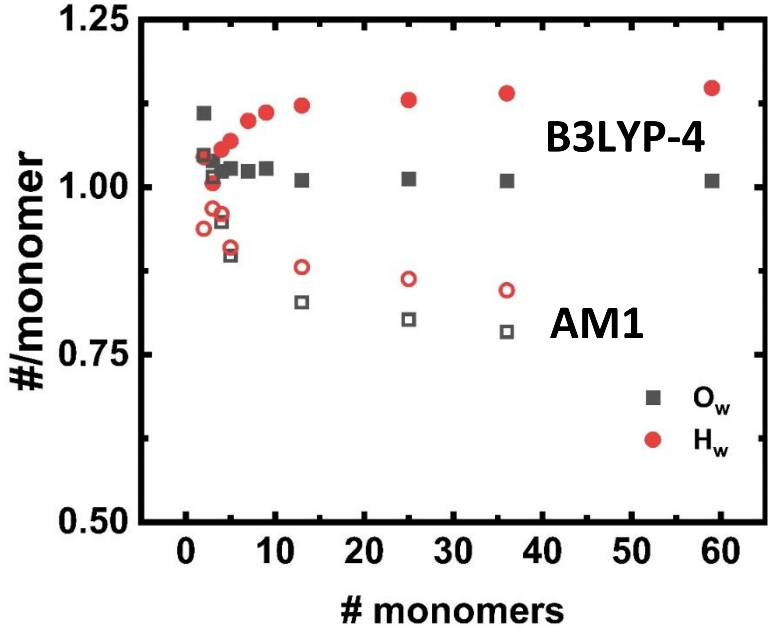

Figure S23: The number of water oxygens (O_w) or hydrogens (H_w) per EO monomer as a function of chain length (# monomers) for both PEO molecules with fixed charges from B3LYP-4 (closed symbols) and AM1 (open symbols). A distance criterion is used to count the number of O_W and H_w within the first hydration shell of PEO and near O_{EO}. The distance cutoffs for $O_w - O_{EO}$ and $H_w - O_{EO}$ are 3.2 and 2.5 Angstroms, respectively; these are typical of values used in the literature and correspond to the minimum past the first peak in the radial distribution functions for $O_w - O_{EO}$ and $H_w - O_{EO}$. Notably, there are fewer waters near the PEO chains for the less polar AM1 charged molecules.

Section 12: 1,2-dimethoxyethane dihedral populations and helicity

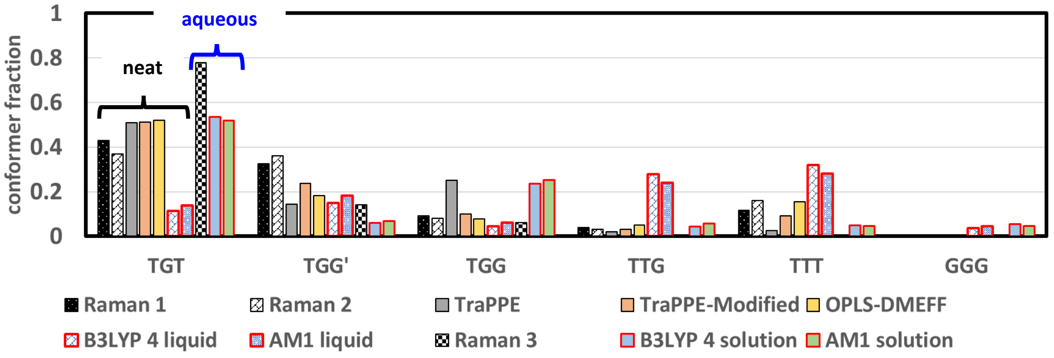

Figure S24: Dihedral confirmer populations for 1,2-dimethoxyethane (PEO 2-mer) for this work (outlined in red) compared to experimental Raman data and other PEO force-fields. Literature simulation data is neat EO_2 at 298K and atmospheric pressure.[25] Raman 1[41] and Raman 2 are data for neat EO_2,[42] and Raman 3 is data for EO_2 in water at a mole fraction of 0.02.[42] All experimental data collected near room temperature, 298-300K, and at atmospheric pressure.

We calculate and analyze dihedral sequences in chains beyond a PEO 2-mer (**SI Section 12**) and report the number of dihedral angles involved in trans-gauche-trans (tgt) sequences along the chain backbone as a function of molecular weight and charge assignment. For example, **-tgttgttg**gg**gtt**t- involves 14 unique dihedrals. Of these 14 only 11 of them are involved in sequences consistent with -tgt- patterning, which are found patterned in two sets: one with 8 (**tgttgttg**) and one with 3 (**gtt**). Of these two sets, one has 6 distinct sets of tri-dihedrals ($l = 6$) and the other 1 ($l = 1$). The total number of sets of tri-dihedrals in this sequence is 12 with only 7 patterned in sequences of interests ($n = 7$, $f = 7/12 = 0.583$). Only -tgt- sequences with the gauche conformation around the C-C bond are counted, and do not distinguish the two degenerate gauche conformations around the C-C bond. We present the average n (n_{avg}), f, and l below as a function of chain length and for both B3LYP4 and AM1 charging.

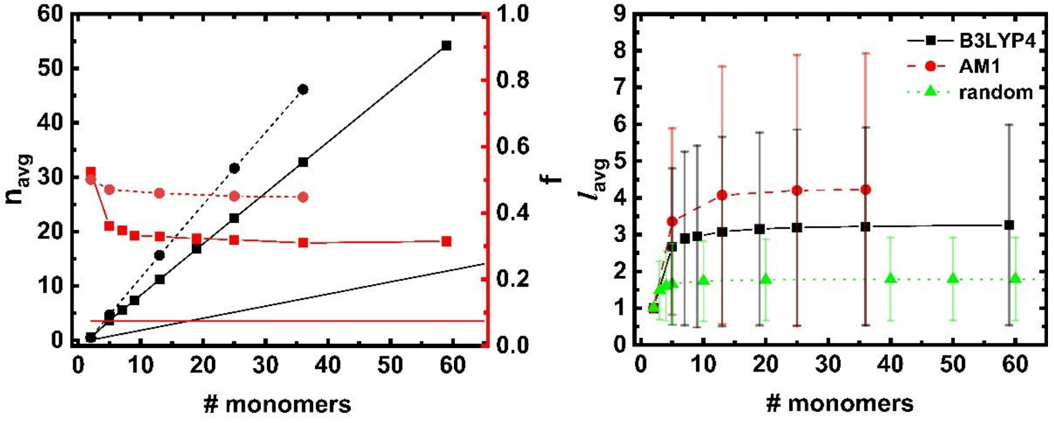

Figure S25: **(left)** The average number of tri-dihedral sequences (n_{avg}) consistent with a -tgt- sequence along the PEO backbone chain, and the fraction (f) of all tri-dihedral sequences that are consistent with a -tgt- patterning (B3LYP and AM1 denoted by square and circle symbols, respectively). The lines without symbols are calculated from generating random dihedral patterns for the same number of monomers. **(right)** The average number of tri-dihedral patterns comprising a sequence with the bars denoting ± 1 standard deviation. Again, the average length of tri-dihedral patterns is also presented for polymers of varying length with random dihedrals to serve as a baseline.

Section 13: α

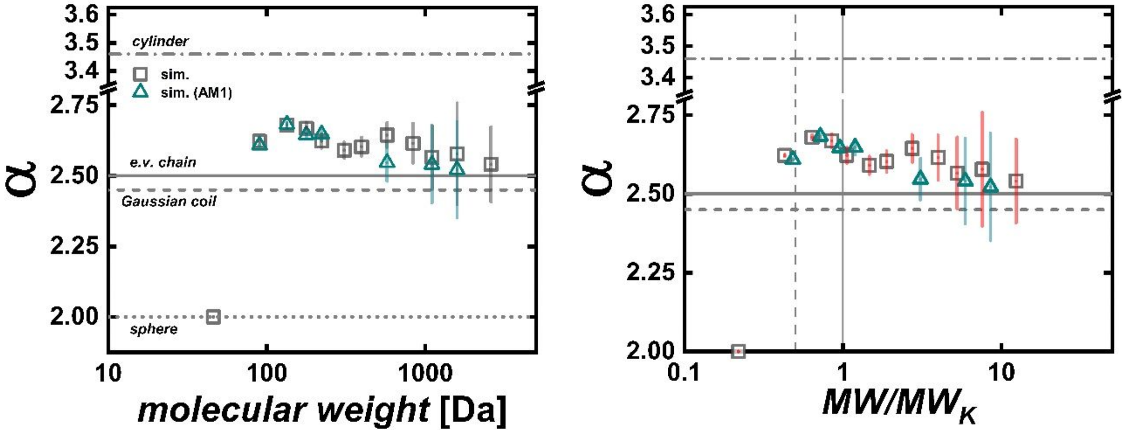

Figure S26: The α, $\sqrt{\langle R_{ee}^2\rangle/\langle R_g^2\rangle}$, value of PEO calculated from the MD simulations. (**right**) The x-axis scaled by the molecular weight corresponding to a Kuhn segment. The error bars represent ± 1 standard error; note the error in both $\tilde{R}_{ee}$ and $\tilde{R}_g$ is compounded in the calculation of α leading to larger error bars.

Section 14: Scaled distribution moments

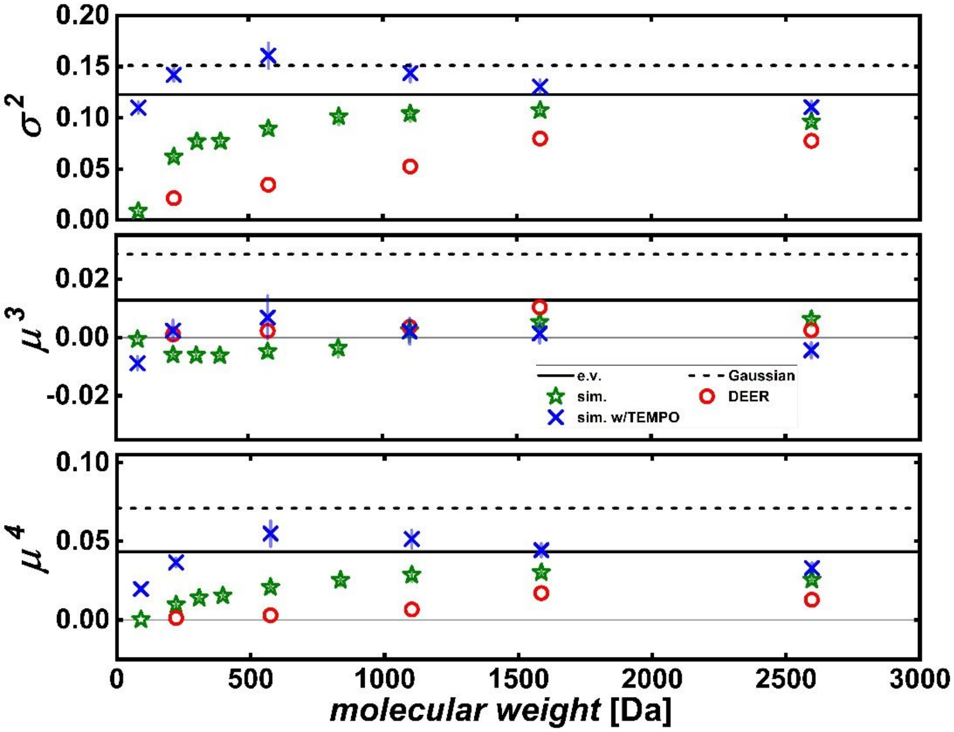

Figure S27: The second, third and fourth moments of the scaled, end-to-end distance probability distributions in **Figure 4**. The solid and dashed lines are the moments numerically calculated from the universal distributions for excluded volume, e.v., and ideal chains, respectively. Error bars are +/- 1 standard deviation.

In addition to the second and third moments, we report the fourth moment here as well. Most important is that the DEER data can detect the increasing importance of the tails between chains of varying length, even if information about possible probe aggregation is missing. As expected, the MD data for the labeled chains has a peak at the 13mer, the tipping point between which the end aggregation beings to decrease rapidly with increasing molecular weight.

Section 15: References

(1) Doll, A.; Qi, M.; Godt, A.; Jeschke, G. CIDME: Short Distances Measured with Long Chirp Pulses. *Journal of Magnetic Resonance* **2016**, *273*, 73–82. https://doi.org/10.1016/j.jmr.2016.10.011.

(2) Banham, J. E.; Baker, C. M.; Ceola, S.; Day, I. J.; Grant, G. H.; Groenen, E. J. J.; Rodgers, C. T.; Jeschke, G.; Timmel, C. R. Distance Measurements in the Borderline Region of Applicability of CW EPR and DEER: A Model Study on a Homologous Series of Spin-Labelled Peptides. *Journal of Magnetic Resonance* **2008**, *191* (2), 202–218. https://doi.org/10.1016/j.jmr.2007.11.023.

(3) Jeschke, G. DEER Distance Measurements on Proteins. *Annu. Rev. Phys. Chem.* **2012**, *63* (1), 419–446. https://doi.org/10.1146/annurev-physchem-032511-143716.

(4) Schweiger, A.; Jeschke, G. *Principles of Pulse Electron Paramagnetic Resonance*; Oxford University Press, 2001.

(5) Altenbach, C. *LongDistances*; 2019.

(6) Chiang, Y.-W.; Borbat, P. P.; Freed, J. H. The Determination of Pair Distance Distributions by Pulsed ESR Using Tikhonov Regularization. *Journal of Magnetic Resonance* **2005**, *172* (2), 279–295. https://doi.org/10.1016/j.jmr.2004.10.012.

(7) Edwards, T. H.; Stoll, S. Optimal Tikhonov Regularization for DEER Spectroscopy. *Journal of Magnetic Resonance* **2018**, *288*, 58–68. https://doi.org/10.1016/j.jmr.2018.01.021.

(8) Brandon, S.; Beth, A. H.; Hustedt, E. J. The Global Analysis of DEER Data. *Journal of Magnetic Resonance* **2012**, *218*, 93–104. https://doi.org/10.1016/j.jmr.2012.03.006.

(9) Srivastava, M.; Freed, J. H. Singular Value Decomposition Method to Determine Distance Distributions in Pulsed Dipolar Electron Spin Resonance. *J. Phys. Chem. Lett.* **2017**, *8* (22), 5648–5655. https://doi.org/10.1021/acs.jpclett.7b02379.

(10) Srivastava, M.; Freed, J. H. Singular Value Decomposition Method To Determine Distance Distributions in Pulsed Dipolar Electron Spin Resonance: II. Estimating Uncertainty. *J. Phys. Chem. A* **2019**, *123* (1), 359–370. https://doi.org/10.1021/acs.jpca.8b07673.

(11) Edwards, T. H.; Stoll, S. A Bayesian Approach to Quantifying Uncertainty from Experimental Noise in DEER Spectroscopy. *Journal of Magnetic Resonance* **2016**, *270*, 87–97. https://doi.org/10.1016/j.jmr.2016.06.021.

(12) Fábregas Ibáñez, L.; Jeschke, G.; Stoll, S. DeerLab: A Comprehensive Toolbox for Analyzing Dipolar EPR Spectroscopy Data. *Magnetic Resonance Discussions* **2020**, 1–28. https://doi.org/10.5194/mr-2020-13.

(13) *Avogadro: An Open-Source Molecular Builder and Visualization Tool.*

(14) Wang, J.; Wolf Romain, M.; Caldwell James, W.; Kollman Peter, A.; Case David, A. Development and Testing of a General Amber Force Field. *Journal of Computational Chemistry* **2004**, *25* (9), 1157–1174. https://doi.org/10.1002/jcc.20035.

(15) Frisch, M. J.; Trucks, G. W.; Schlegel, H. B.; Scuseria, G. E.; Robb, M. A.; Cheeseman, J. R.; Scalmani, G.; Barone, V.; Petersson, G. A.; Nakatsuji, H.; Li, X.; Caricato, M.; Marenich, A. V.; Bloino, J.; Janesko, B. G.; Gomperts, R.; Mennucci, B.; Hratchian, H. P.; Ortiz, J. V.; Izmaylov, A. F.; Sonnenberg, J. L.; Williams; Ding, F.; Lipparini, F.; Egidi, F.; Goings, J.; Peng, B.; Petrone, A.; Henderson, T.; Ranasinghe, D.; Zakrzewski, V. G.; Gao, J.; Rega, N.; Zheng,

G.; Liang, W.; Hada, M.; Ehara, M.; Toyota, K.; Fukuda, R.; Hasegawa, J.; Ishida, M.; Nakajima, T.; Honda, Y.; Kitao, O.; Nakai, H.; Vreven, T.; Throssell, K.; Montgomery Jr., J. A.; Peralta, J. E.; Ogliaro, F.; Bearpark, M. J.; Heyd, J. J.; Brothers, E. N.; Kudin, K. N.; Staroverov, V. N.; Keith, T. A.; Kobayashi, R.; Normand, J.; Raghavachari, K.; Rendell, A. P.; Burant, J. C.; Iyengar, S. S.; Tomasi, J.; Cossi, M.; Millam, J. M.; Klene, M.; Adamo, C.; Cammi, R.; Ochterski, J. W.; Martin, R. L.; Morokuma, K.; Farkas, O.; Foresman, J. B.; Fox, D. J. *Gaussian 16 Rev. B.01*; Wallingford, CT, 2016.

(16) *AmberTools18*.

(17) Bayly, C. I.; Cieplak, P.; Cornell, W.; Kollman, P. A. A Well-Behaved Electrostatic Potential Based Method Using Charge Restraints for Deriving Atomic Charges: The RESP Model. *The Journal of Physical Chemistry* **1993**, *97* (40), 10269–10280. https://doi.org/10.1021/j100142a004.

(18) Wang, J.; Wang, W.; Kollmann, P.; Case, D. Antechamber, An Accessory Software PackageFor Molecular Mechanical Calculation. *J. Comput. Chem.* **//**, *25*, 1157–1174.

(19) Jakalian, A.; Bush, B. L.; Jack, D. B.; Bayly, C. I. Fast, Efficient Generation of High-Quality Atomic Charges. AM1-BCC Model: I. Method. *Journal of Computational Chemistry* **2000**, *21* (2), 132–146. https://doi.org/10.1002/(SICI)1096-987X(20000130)21:2<132::AID-JCC5>3.0.CO;2-P.

(20) Jakalian, A.; Jack, D. B.; Bayly, C. I. Fast, efficient generation of high-quality atomic charges. AM1-BCC model: II. Parameterization and validation https://onlinelibrary.wiley.com/doi/abs/10.1002/jcc.10128 (accessed Jul 26, 2019).

(21) Barbosa, N. S. V.; Zhang, Y.; Lima, E. R. A.; Tavares, F. W.; Maginn, E. J. Development of an AMBER-Compatible Transferable Force Field for Poly(Ethylene Glycol) Ethers (Glymes). *Journal of Molecular Modeling* **2017**, *23* (6), 194. https://doi.org/10.1007/s00894-017-3355-3.

(22) Henni, A.; Naami, A.; Tontiwachwuthikul, P. Densities, Viscosities, and Derived Functions of Binary Mixtures: (Triethylene Glycol Dimethyl Ether + Water) and (N-Acetylmorpholine + Water) from 298.15 K to 343.15 K. *Journal of Chemical & Engineering Data* **2005**, *50* (3), 1038–1042. https://doi.org/10.1021/je050021e.

(23) McGee, R. L.; Wallace, W. J.; Rataiczak, R. D. Densities, Viscosities, Refractive Indexes, and Molar Refractions of the Binary System Tetraethylene Glycol Dimethyl Ether-Water at 25.Degree.C. *Journal of Chemical & Engineering Data* **1983**, *28* (3), 305–307. https://doi.org/10.1021/je00033a006.

(24) Devanand, K.; Selser, J. C. Asymptotic Behavior and Long-Range Interactions in Aqueous Solutions of Poly(Ethylene Oxide). *Macromolecules* **1991**, *24* (22), 5943–5947. https://doi.org/10.1021/ma00022a008.

(25) Fischer, J.; Paschek, D.; Geiger, A.; Sadowski, G. Modeling of Aqueous Poly(Oxyethylene) Solutions: 1. Atomistic Simulations. *The Journal of Physical Chemistry B* **2008**, *112* (8), 2388–2398. https://doi.org/10.1021/jp0765345.

(26) Wang, Y.-L.; Lawrence, R. S.; Lu, Z.-Y.; Laaksonen, A. Molecular Dynamics Study of Aqueous Solution of Polyethylene Oxide: Critical Test of Force Field Models. *Soft Materials* **2013**, *11* (4), 371–383. https://doi.org/10.1080/1539445X.2012.669221.

(27) Lee, H.; Venable, R. M.; MacKerell, A. D.; Pastor, R. W. Molecular Dynamics Studies of Polyethylene Oxide and Polyethylene Glycol: Hydrodynamic Radius and Shape Anisotropy.

Biophysical Journal **2008**, *95* (4), 1590–1599. https://doi.org/10.1529/biophysj.108.133025.

(28) Kawaguchi, S.; Imai, G.; Suzuki, J.; Miyahara, A.; Kitano, T.; Ito, K. Aqueous Solution Properties of Oligo- and Poly(Ethylene Oxide) by Static Light Scattering and Intrinsic Viscosity. *Polymer* **1997**, *38* (12), 2885–2891. https://doi.org/10.1016/S0032-3861(96)00859-2.

(29) Stuart, M. A. C.; Waajen, F. H. W. H.; Cosgrove, T.; Vincent, B.; Crowley, T. L. Hydrodynamic Thickness of Adsorbed Polymer Layers. *Macromolecules* **1984**, *17* (9), 1825–1830. https://doi.org/10.1021/ma00139a035.

(30) Le Cœur, C.; Combet, S.; Carrot, G.; Busch, P.; Teixeira, J.; Longeville, S. Conformation of the Poly(Ethylene Glycol) Chains in DiPEGylated Hemoglobin Specifically Probed by SANS: Correlation with PEG Length and in Vivo Efficiency. *Langmuir* **2015**, *31* (30), 8402–8410. https://doi.org/10.1021/acs.langmuir.5b01121.

(31) Polverari, M.; van de Ven, T. G. M. Dilute Aqueous Poly(Ethylene Oxide) Solutions: Clusters and Single Molecules in Thermodynamic Equilibrium. *The Journal of Physical Chemistry* **1996**, *100* (32), 13687–13695. https://doi.org/10.1021/jp960215o.

(32) Alessi, M. L.; Norman, A. I.; Knowlton, S. E.; Ho, D. L.; Greer, S. C. Helical and Coil Conformations of Poly(Ethylene Glycol) in Isobutyric Acid and Water. *Macromolecules* **2005**, *38* (22), 9333–9340. https://doi.org/10.1021/ma051339e.

(33) Rubinson, K. A.; Krueger, S. Poly(Ethylene Glycol)s 2000–8000 in Water May Be Planar: A Small-Angle Neutron Scattering (SANS) Structure Study. *Polymer* **2009**, *50* (20), 4852–4858. https://doi.org/10.1016/j.polymer.2009.08.023.

(34) Petrenko, V.; Bulavin, L.; Avdeev, M.; Garamus, V.; Koneracka, M.; Kopcansky, P. Structure and Interaction of Poly(Ethylene Glycol) in Aqueous Solutions. Small-Angle Neutron Scattering Data. *Macromolecular Symposia* **2014**, *335* (1), 20–23. https://doi.org/10.1002/masy.201200117.

(35) Lancz, G.; Avdeev, M. V.; Petrenko, V. I.; Garamus, V. M.; Koneracká, M.; Kopčanský, P. SANS Study of Poly(Ethylene Glycol) Solutions in D_2O. *Acta Phys. Pol. A* **2010**, *118* (5), 980–982. https://doi.org/10.12693/APhysPolA.118.980.

(36) Watkins, H. M.; Simon, A. J.; Sosnick, T. R.; Lipman, E. A.; Hjelm, R. P.; Plaxco, K. W. Random Coil Negative Control Reproduces the Discrepancy between Scattering and FRET Measurements of Denatured Protein Dimensions. *Proc Natl Acad Sci U S A* **2015**, *112* (21), 6631–6636. https://doi.org/10.1073/pnas.1418673112.

(37) Rubinstein, M.; Colby, R. H. *Polymer Physics*; Oxford University Press: USA, 2003.

(38) Dahal, U. R.; Dormidontova, E. E. The Dynamics of Solvation Dictates the Conformation of Polyethylene Oxide in Aqueous, Isobutyric Acid and Binary Solutions. *Phys. Chem. Chem. Phys.* **2017**, *19* (15), 9823–9832. https://doi.org/10.1039/C7CP00526A.

(39) Dittmore, A.; McIntosh, D. B.; Halliday, S.; Saleh, O. A. Single-Molecule Elasticity Measurements of the Onset of Excluded Volume in Poly(Ethylene Glycol). *Physical Review Letters* **9**, *107* (14), 148301. https://doi.org/10.1103/PhysRevLett.107.148301.

(40) Mark, J. E.; Flory, P. J. The Configuration of the Polyoxyethylene Chain. *Journal of the American Chemical Society* **1965**, *87* (7), 1415–1423. https://doi.org/10.1021/ja01085a001.

(41) Goutev, N.; Ohno, K.; Matsuura, H. Raman Spectroscopic Study on the Conformation of 1,2-Dimethoxyethane in the Liquid Phase and in Aqueous Solutions. *J. Phys. Chem. A* **2000**, *104* (40), 9226–9232. https://doi.org/10.1021/jp001340+.

(42) Wada, R.; Fujimoto, K.; Kato, M. Why Is Poly(Oxyethylene) Soluble in Water? Evidence from the Thermodynamic Profile of the Conformational Equilibria of 1,2-Dimethoxyethane and Dimethoxymethane Revealed by Raman Spectroscopy. *The Journal of Physical Chemistry B* **2014**, *118* (42), 12223–12231. https://doi.org/10.1021/jp5048997.